Journal of
METAMORPHIC GEOLOGY

J. metamorphic Geol., 2011 doi:10.1111/j.1525-1314.2011.00932.x

Metamorphic evolution, partial melting and rapid exhumation above an ancient flat slab: insights from the San Emigdio Schist, southern California

A. D. CHAPMAN,[1] P. I. LUFFI,[2] J. B. SALEEBY[1] AND S. PETERSEN[3]
[1]*Division of Geological and Planetary Sciences, California Institute of Technology, M/C 100-23 1200 E. California Blvd., Pasadena, CA 91125, USA (alan@gps.caltech.edu)*
[2]*Department of Earth Science, Rice University MS-126, 6100 Main St., Houston, TX 77005, USA*
[3]*Department of Earth and Planetary Sciences, Harvard University, 20 Oxford St., Cambridge, MA 02138, USA*

ABSTRACT The San Emigdio and related Pelona, Orocopia, Rand and Sierra de Salinas schists of southern California were underplated beneath the southern Sierra Nevada batholith and adjacent southern California batholith along a shallow segment of the subducting Farallon plate in Late Cretaceous to early Tertiary time. These subduction accretion assemblages represent a regional, deeply exhumed, shallowly dipping domain from an ancient slab segmentation system and record the complete life cycle of the segmentation process from initial flattening and compression to final extensional collapse. An important unresolved question regarding shallow subduction zones concerns how the thermal structure evolves during the slab flattening process. New field relationships, thermobarometry, thermodynamic modelling and garnet diffusion modelling are presented that speak to this issue and elucidate the tectonics of underplating and exhumation of the San Emigdio Schist. We document an upsection increase in peak temperature (i.e. inverted metamorphism), from 590 to 700 °C, peak pressures ranging from 8.5 to 11.1 kbar, limited partial melting, microstructural evidence for large seismic events, rapid cooling (825–380 °C Myr^{-1}) from peak conditions and an 'out and back' *P–T* path. While inverted metamorphism is a characteristic feature of southern California schists, the presence of partial melt and high temperatures (>650 °C) are restricted to exposures with maximum depositional ages between 80 and 90 Ma. Progressive cooling and tectonic underplating beneath an initially hot upper plate following the onset of shallow subduction provide a working hypothesis explaining high temperatures and partial melting in San Emigdio and Sierra de Salinas schists, inverted metamorphism in the schist as a whole, and the observed *P–T* trajectory calculated from the San Emigdio body. Lower temperatures in Pelona, Orocopia and Rand schists are likewise explained in the context of this overarching model. These results are consistent with an inferred tectonic evolution from shallow subduction beneath the then recently active Late Cretaceous arc to exhumation by rapid trench-directed channelized extrusion in the subducted schist.

Key words: diffusion modelling; garnet; inverted metamorphism; *P–T* pseudosections; San Emigdio Schist.

INTRODUCTION

Crustal rocks are subducted along a variety of trajectories into the mantle. For instance, along-strike variations in slab dip have resulted in the concomitant formation of the high-pressure/low-temperature Franciscan complex and the high-pressure/moderate- to high-temperature Pelona, Orocopia, Rand, San Emigdio and Sierra de Salinas schist (collectively referred to as 'the southern California schist') terrane in California (Fig. 1) (Grove *et al.*, 2003; Wakabayashi & Dumitru, 2007). While the Middle Mesozoic to early Tertiary Franciscan complex is thought to be the product of moderately dipping subduction, the Late Cretaceous to early Tertiary southern California schist was underplated directly beneath the southern Sierra Nevada batholith (SNB) and the once contiguous southern California batholith (granitoids of the Mojave–Salinia region) along a comparatively shallowly dipping segment of the subducting Farallon plate (Jacobson *et al.*, 2007 and references therein). The deposition, subduction and structural ascent of the schist are temporally and spatially associated in plate reconstructions with the subduction of the eastern conjugate massif to the Shatsky Rise, a large igneous province (LIP) ~2000 km south-east of Japan (Saleeby, 2003; Liu *et al.*, 2008, 2010). Subduction of the LIP is hypothesized to have driven slab flattening and upper plate extension (Saleeby

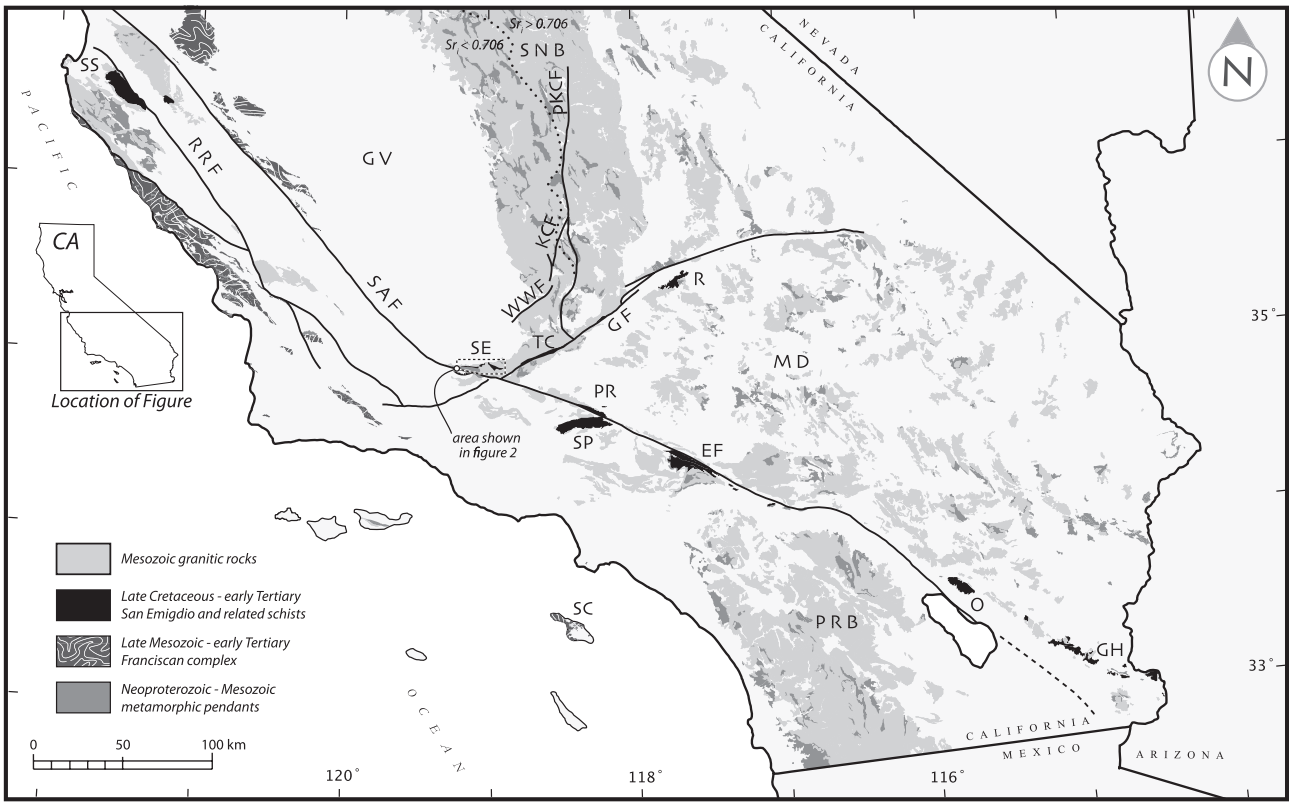

Fig. 1. Geological map of southern California basement rocks based on USGS Open-File Report 2005-1305 (Ludington *et al.*, 2007). EF, East Fork (San Gabriel Mountains); GF, Garlock fault; GH, Gavilan Hills; GV, Great Valley; KCF, Kern Canyon fault; MD, Mojave Desert; O, Orocopia Mountains; PRB, Peninsular Ranges batholith; PR, Portal Ridge; pKCF, proto-Kern Canyon fault; R, Rand Mountains; RRF, Reliz–Rinconada fault; SAF, San Andreas fault; SE, San Emigdio Mountains; SC, Santa Catalina Island; SNB, Sierra Nevada batholith; SP, Sierra Pelona; SS, Sierra de Salinas; TC, Tehachapi Mountains; WWF, White Wolf fault.

et al., 2007; Chapman *et al.*, 2010) somewhat analogous to the ongoing subduction of the Nazca Ridge and trench-directed detachment faulting above the Peruvian flat slab segment (Gutscher *et al.*, 2000; McNulty & Farber, 2002).

An along-strike inflection zone varying from shallower to steeper slab dips northwestward, approximately centred along the trace of the superimposed Garlock fault (Saleeby, 2003), separates the schist and Franciscan subduction accretion assemblages, respectively (Fig. 1). Deep-crustal batholithic exposures, subjacent schist, and an intervening shear zone (the Rand fault and Salinas shear zone) of the southern Sierra Nevada, the adjacent north-west Mojave Desert, and the northern Salinia terrane (prior to Neogene northward translation) offer a unique opportunity to observe the inflection zone above a segmented slab. Furthermore, this package records a complete life cycle of the segmentation process with initial flattening resulting in the upper plate mantle lithosphere removal coincident with compressional deformation, rock uplift and denudation, followed abruptly by extensional collapse, all occurring in series as subduction progressed (Saleeby *et al.*, 2007). An important unresolved question regarding shallow subduction zones concerns how the thermal structure evolves during the slab flattening process (English *et al.*, 2003; Kidder & Ducea, 2006). We address this issue through petrogenetic characterization of the earliest formed schist in the San Emigdio Mountains, and comparison of this schist with later formed Pelona, Orocopia, Rand and Sierra de Salinas members.

Metasandstone and metabasaltic rocks of the San Emigdio Schist are distinguished from exposures of related Pelona, Orocopia, Rand and Sierra de Salinas schists by the nearly ubiquitous presence of garnet porphyroblasts. Growth zonation in these garnet grains is well-preserved, allowing for straightforward recovery of a portion of the pressure–temperature (*P–T*) history of the shallowly subducted schist (e.g. Spear & Selverstone, 1983; Vance & Mahar, 1998; Escuder Viruete *et al.*, 2000). In addition, some garnet experienced cataclastic deformation. Subsequent overgrowth along broken margins resulted in natural diffusion couples from which the duration of metamorphic processes may be derived (e.g. Chakraborty & Ganguly, 1991; Ganguly *et al.*, 1996; Dachs & Proyer, 2002; Ganguly, 2002; Vielzeuf *et al.*, 2007). New field relationships, thermobarometry, thermodynamic modelling and garnet diffusion modelling are

presented here that constrain the *P–T* history and the tectonics of underplating and exhumation of the San Emigdio Schist. These observations constrain the physical conditions once present above the Farallon flat slab segment and further our understanding of the tectonics of slab flattening and schist underthrusting and exhumation in the southern California region.

GEOLOGICAL BACKGROUND

The southern California schist has long attracted interest due to its position structurally beneath older Mesozoic batholithic rocks throughout southern California (Graham & England, 1976; Haxel & Dillon, 1978; Ehlig, 1981; Jacobson, 1983, 1995; Jacobson *et al*., 1988, 2007, 2011). Most workers agree that the deposition and emplacement of the schist occurred during an episode of shallow subduction related to the Laramide orogeny (Jacobson *et al*., 2007 and references therein). Geochronological, thermochronometric and thermobarometric studies indicate a temporal link between schist unroofing and major upper crustal extension (Pickett & Saleeby, 1993; Jacobson, 1995; Kistler & Champion, 2001; Barth *et al*., 2003; Grove *et al*., 2003; Kidder *et al*., 2003; Kidder & Ducea, 2006; Saleeby *et al*., 2007). Existing models for the exhumation of the northern (i.e. Rand and Sierra de Salinas) and southern (i.e. Pelona and Orocopia) schists invoke return flow (Oyarzabal *et al*., 1997; Jacobson *et al*., 2002; Saleeby, 2003; Saleeby *et al*., 2007; Chapman *et al*., 2010), isostatically driven uplift (Jacobson *et al*., 2007), upper plate normal faulting (e.g. Jacobson *et al*., 1996), erosion (Yin, 2002) or some combination thereof. In the San Emigdio and Tehachapi Mountains, trench-directed channelized extrusion in the subducted schist is hypothesized to have led to collapse of the upper plate between *c*. 98 and 86 Ma (Saleeby *et al*., 2007; Chapman *et al*., 2010).

Uplift and folding of basement rocks and sedimentary cover strata in the San Emigdio Mountains were controlled by Pliocene–Quaternary north–south compression between the big bend in the San Andreas fault and the Pleito fault zone (Fig. 2) (Dibblee, 1986). A semi-continuous belt of southern California schist constitutes the base of the tectonic section in the San Emigdio and Tehachapi Mountains (referred to as 'Pelona Schist' by Sharry, 1981; 'Rand Schist' by Grove *et al*., 2003; Saleeby *et al*., 2007; Chapman *et al*., 2010; and 'San Emigdio Schist' by Jacobson *et al*., 2011). We follow the usage of Jacobson *et al*. (2011) and present evidence here that the San Emigdio Schist is distinct from other southern California members on the basis of geography, petrology and detrital zircon age distribution.

The Tehachapi–San Emigdio (TSE) complex structurally overlies the San Emigdio Schist and consists of a series of Early to mid-Cretaceous deep-level plutonic rocks and associated pre-Cretaceous framework metamorphic rocks (Saleeby *et al*., 2007; Chapman *et al*., 2010). The San Emigdio Schist is juxtaposed against the TSE complex along the remains of a locally ductile to brittle low-angle detachment fault system that probably correlates with the type Rand fault exposed in the Rand Mountains (Postlethwaite & Jacobson, 1987). During Pliocene–Quaternary compression, the Rand fault in the San Emigdio Mountains was largely folded with a major south-dipping thrust fault cutting across the folded structural section. As a result, the tectonostratigraphy is inverted with the San Emigdio Schist in the hangingwall and the TSE complex in the footwall. Decompression of the San Emigdio Schist from deep- to mid-crustal levels is well constrained at 91–86 Ma (Grove *et al*., 2003) and is linked to extensional deformation along the Rand fault (Saleeby *et al*., 2007). The TSE complex structurally underlies the Pastoria plate along the Late Cretaceous to Eocene (?) (Wood & Saleeby, 1997) south-dipping Pastoria detachment. The Pastoria plate is composed of relatively shallow level (3–4 kbar) eastern SNB affinity granitoids and metamorphic pendant rocks (Crowell, 1952).

METAMORPHIC PETROLOGY

Mineral abbreviations: Act, actinolite; alm, almandine; And, andalusite; Bt, biotite; Chl, chlorite; Cpx, clinopyroxene; Crd, cordierite; Cum, cummingtonite; Ep, epidote; Fsp, feldspar; Grt, garnet; Gln, glaucophane; Gr, graphite; grs, grossular; Hbl, hornblende; Ilm, Ilmenite; Kfs, K-feldspar; Ky, kyanite; Lws, lawsonite; Ms, muscovite; Omp, omphacite; Opx, orthopyroxene; Pg, paragonite; Pl, plagioclase; prp, pyrope; Qz, quartz; Rt, rutile; Sil, sillimanite; sps, spessartine; Spn, sphene; St, staurolite; Zo, zoisite.

Tehachapi–San Emigdio complex

The TSE complex in the upper plate of the Rand fault in San Emigdio Mountains consists of at least two distinct upper amphibolite facies orthogneiss units (Fig. 2) and one paragneiss unit. These include: (i) the 131 Ma Antimony Peak tonalite (James, 1986), (ii) an undated hornblende quartz diorite gneiss that probably correlates with hornblende gabbroids of the 105–99 Ma intrusive suite of Bear Valley (Saleeby *et al*., 1987, 2007; Pickett & Saleeby, 1993) and (iii) the western continuation of the Grapevine Canyon paragneiss (Pickett & Saleeby, 1993, 1994).

The Antimony Peak body is a medium- to coarse-grained massive to penetratively foliated tonalite that contains mainly plagioclase, quartz, hornblende and K-feldspar, with minor amounts of garnet, biotite, epidote, apatite, sphene and ilmenite (Fig. 3a). Where hypidiomorphic granular (igneous) textures are not overprinted by metamorphic foliation, the epidote occurs as subhedral replacement products of embayed hornblende and retains distinct core and rim regions, consistent with a magmatic origin. Original petrographic relationships are locally obscured by extensive seritization and chloritization.

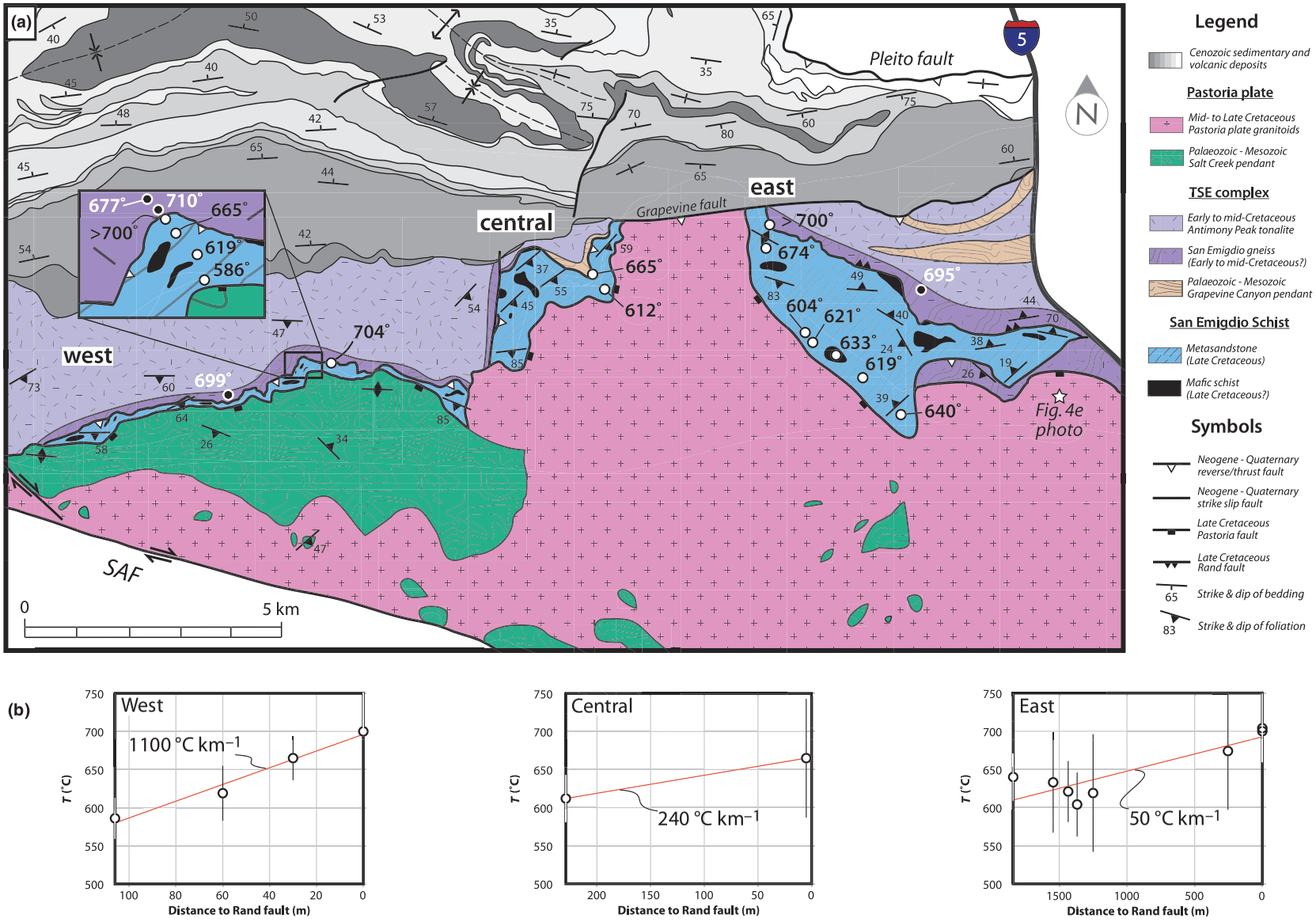

Fig. 2. (a) Simplified geological map of the San Emigdio Mountains. Geology from Ross (1989), Dibblee (1973), Chapman *et al.* (2010) and this study. Mafic schist shown in black. Black and white circles show locations of thermobarometric determinations from upper plate and San Emigdio Schist, respectively. Abbreviations as in Fig. 1. (b) Graphical representation of thermometric data along western, central and eastern transects.

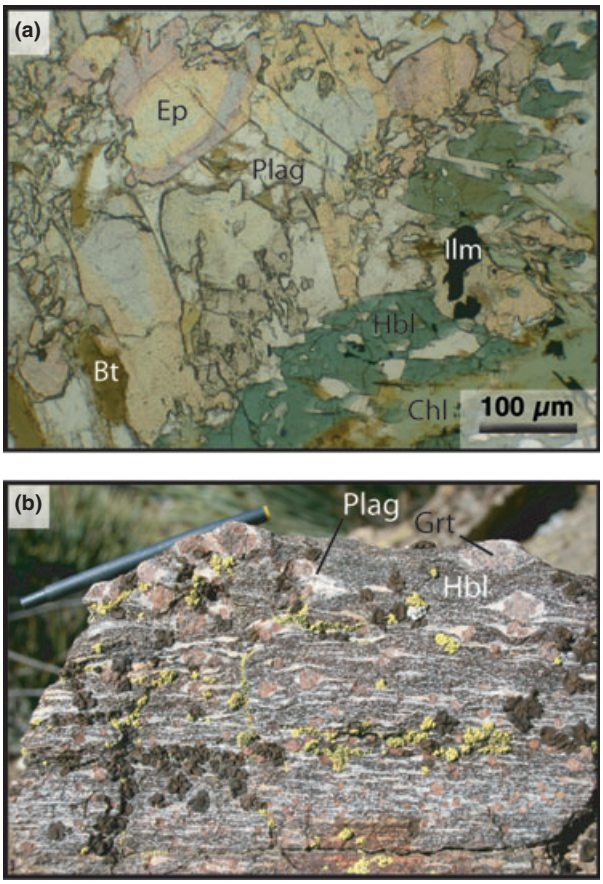

Fig. 3. Photographs of petrological features in the TSE complex. (a) Magmatic epidote in Antimony Peak tonalite; ppl. (b) Field photograph showing textural relations of garnet formation in San Emigdio gneiss. ppl, plane-polarized light.

The second unit is informally named the San Emigdio quartz diorite orthogneiss and abbreviated the San Emigdio gneiss (Fig. 3b). The San Emigdio gneiss lies structurally above the Rand fault, and consequently exhibits a strongly attenuated structural fabric characterized by anastomosing ductile to brittle shear zones. We consider the San Emigdio gneiss a tectonic unit that consists mainly of strongly sheared quartz diorite: hornblende + plagioclase + quartz + ilmenite ± coarse subsolidus garnet ± sphene ± K-feldspar, with lesser amounts of deformed tonalite and trondhjemite. The upper plate thermobarometric work was focussed primarily on the San Emigdio gneiss, as this unit lies in structural contact with the San Emigdio Schist.

San Emigdio Schist

The San Emigdio Schist consists of roughly 80% interlayered metapsammite and quartzite (metasandstone) commingled with 15% metabasalt and 5% ultramafic (talc–actinolite) schist (Fig. 4). The metasandstone member of the schist is characterized by the well-preserved peak mineral paragenesis garnet + plagioclase + biotite + quartz ± muscovite ± kyanite, which defines the D1 foliation, a weakly crenulated fabric with lesser amounts of rutile, ilmenite and graphite. In addition, mineral assemblages and textures vary with structural depth. Highly altered kyanite grains and chloritized kyanite pseudomorphs prevalent at low structural levels of the schist are absent at higher structural levels (Fig. 4). Also, as the Rand fault is approached from low structural levels: (i) garnet size and abundance increases; (ii) plagioclase changes from untwinned, graphitic poikiloblasts to twinned, graphite-free and inclusion-poor porphyroblasts; (iii) primary muscovite disappears; (iv) the overall grain size increases; (v) macroscopic stromatic leucosomes and melanosomes develop within the D1 foliation; and (vi) ductilely deformed quartzofeldspathic (milky quartz + plagioclase ± garnet ± muscovite) veins become more common and more strongly transposed along the D1 foliation (Fig. 4). Observations 5 and 6 suggest that fluid-saturated partial melting occurred during the D1 episode. A less pervasive fabric, D2, is localized within mm-scale non-coaxial shear zones that truncate D1 mineral assemblages and anatectic textures and contain retrograde clinozoisite, chlorite, celadonitic muscovite, tourmaline and highly sheared minerals belonging to the D1 assemblage. Finally, clinozoisite, while only associated with the D2 assemblage at moderate to high structural levels, is a rare D1 phase at deep levels (>1000 m). Therefore, in contrast to high structural levels where amphibolite facies conditions were reached and limited partial melting may have occurred, peak conditions probably did not exceed epidote–amphibolite facies at low structural levels. These observations support thermobarometric work (detailed below) indicating the presence of an inverted metamorphic field gradient.

The metabasalt member, referred to here as 'mafic schist', also records multiple distinct phases of deformation and metamorphism. Epidote relics characterize the earliest preserved phase, occurring as isolated, 2 to 5 mm-long optically continuous inclusions in plagioclase, commonly exhibiting concentric birefringence zonation (Fig. 4). Narrow rims of opaque minerals and small (25–50 μm) ovoid quartz blebs commonly intervene between epidote and host plagioclase. We interpret the textural relationships between plagioclase and epidote to result from epidote breakdown by a reaction such as epidote + quartz $\Rightarrow$ anorthite + opaque + H_2O (Spear, 1993). A D1 fabric is wrapped about epidote porphyroblasts, and is defined by well-preserved elongate tschermakitic to pargasitic hornblende + plagioclase ± quartz and subordinate Ti-oxides ± garnet ± biotite. Plagioclase porphyroblasts are typically homogeneous and range in composition from An_{17} to An_{35} (oligoclase to andesine) from sample to sample. At high structural levels (<100 m from the Rand fault), diopsidic to augitic clinopyroxene enters the stable D1 assemblage (Fig. 4). The D1 fabric is locally overprinted by retrograde D2

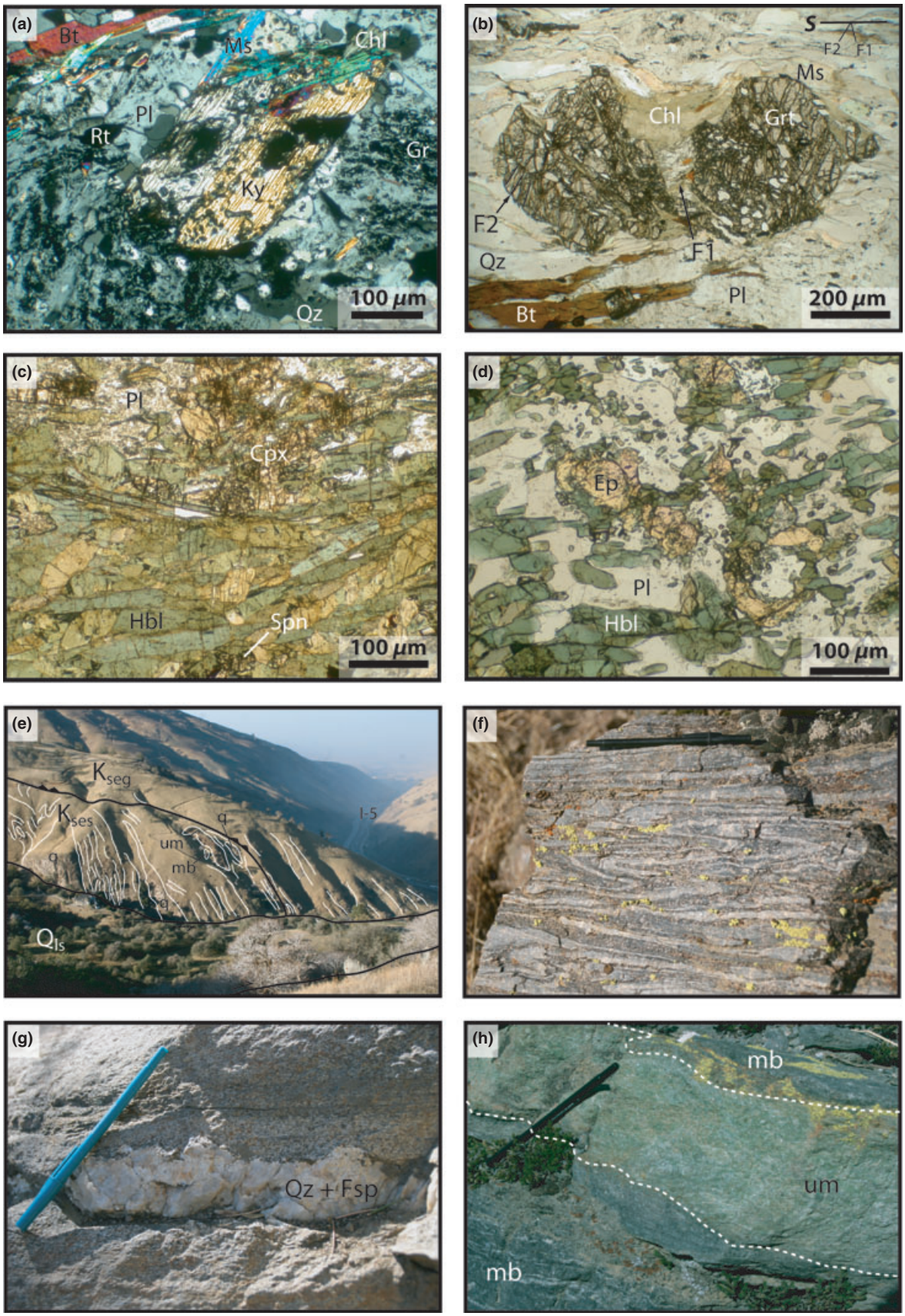

minerals clinozoisite, tremolite and calcite. Retrograde chlorite is rare. Retrograde conversion of hornblende to actinolite, as seen along the Vincent fault in the San Gabriel Mountains (Jacobson, 1997), is not observed. Lenses of ultramafic material typically crop out within or adjacent to mafic schist (Fig. 4).

In contrast to other exposures of the southern California schist (e.g. Sharry, 1981; Postlethwaite & Jacobson, 1987; Jacobson, 1997; Kidder & Ducea, 2006; Jacobson *et al*., 2007), the San Emigdio Schist has abundant garnet except at the lowest structural levels. The majority of garnet from both metasandstone and mafic schist forms 1 to 5 mm idioblastic grains with blebby quartz inclusions. By contrast, within the upper ~150 m of the schist, garnet is locally cataclastically deformed along two sets of fractures, F1 and F2, potentially corresponding to D1 and D2 episodes (Fig. 4). While we cannot conclusively link F1 and F2 fractures to D1 and D2 fabric development, there exists a clear temporal relationship between the fracture sets. Garnet exhibiting F2 fractures is characterized by pervasive, linear, near foliation-normal, dilatant cracks that overprint F1 fractures. Similar features reported from the Morin shear zone of the Canadian Grenville Province are interpreted as evidence of structural ascent in the upper crust (Ji *et al*., 1997). We focus here on garnet exhibiting F1 fractures, and such garnet is hereafter referred to as 'broken garnet'. These garnet grains are either torn completely apart or frictionally displaced along fractured surfaces with no systematic orientation and are partially replaced by D2 minerals. The displacement along fractured surfaces is typically between 50 μm and 2 mm. However, large portions of several broken garnet grains are entirely missing and cannot be recognized in the same thin section. This implies large displacements (>2 mm; comparable to or exceeding the grain size) along fractures regardless of whether missing garnet fragments were dispersed into the third dimension or translated entirely from the thin section.

MINERAL ZONATION

Analytical methods

Electron microprobe analyses were performed using a JEOL8200 system (California Institute of Technology) equipped with five LiF, PET and TAP crystal spectrometers. Major element concentrations were measured in point and line analyses at 15 kV accelerating voltage and a 25 nA beam current with 60 s count times, using natural and synthetic standards, and the CITZAF correction algorithm. Garnet analyses were performed in spot mode, while plagioclase, muscovite and biotite grains were measured using a 5 μm beam width. Individual points along some analytical traverses in garnet were spaced as little as 1 μm apart. At this spacing interval, given the length of our diffusion profile, the effect of spatial averaging in microprobe analysis is negligible compared to the uncertainties in available self-diffusion and interdiffusion data (Ganguly *et al*., 1988). X-ray imaging of Fe, Mg, Ca, Mn, P and Ti distribution in garnet was done with the same instrument at 15 kV accelerating voltage and 400 nA beam current with a pixel size of 5 μm and dwell times of 300 ms per pixel. Maps were processed to enhance zonation features using the imagesc function in MATLAB.

Schist

X-ray mapping and analytical traverses of broken and intact garnet from both metasandstone and mafic schist members (Fig. 5) show well-preserved bell-shaped Mn profiles with Mn-rich core regions and Mn-poor rims, plus monotonically increasing Mg# (Mg/Mg + Fe) from core to rim, features indicative of typical prograde garnet growth (Spear, 1993). However, sharp and pronounced compositional gradients, particularly in Mn and Ca, corresponding to inclusion-rich rims and relatively inclusion-poor cores suggest a two-stage growth history. While a detailed analysis of the growth history of San Emigdio Schist garnet is beyond the scope of this article, we argue below that core-overgrowth textures probably developed during a single metamorphic event as opposed to two discrete events because: (i) steep compositional gradients may be explained by fractional crystallization and (ii) the time interval between deposition, deep subduction (~30 km), and structural ascent to mid-crustal levels was extremely short (<3 Myr) (Grove *et al*., 2003). At high structural levels (<150 m from the Rand fault) in the extreme easternmost and westernmost exposures of the schist in the San Emigdio Mountains, garnet resorption features and diffusive relaxation of major and trace element growth zonation are common (Figs 5 & 6). Except at high structural levels, garnet lacks 'Mn kick-ups' (Kohn & Spear, 2000), indicating that Fe–Mg exchange between garnet and biotite has not been disrupted by retrograde net transfer reactions. Whereas zonation is concentric in idioblastic garnet, there is an obvious truncation, most

Fig. 4. Photographs of structural and petrological features in metasandstone (a, b, f & g) and mafic (c, d & h) San Emigdio schist. (a) Altered kyanite porphyroblast surrounded by graphitic plagioclase poikiloblasts; xpl. (b) Broken garnet porphyroblast exhibiting two sets of fractures corresponding to D1 (F1) and D2 (F2) episodes. Note D2 minerals between garnet fragments; ppl. (c) Coexisting diopsidic clinopyroxene and hornblende at high structural levels; ppl. (d) Epidote relic; ppl. (e) View north from Digier Canyon (star in Fig. 2) of commingled metasandstone (not labelled), quartzite (q), mafic (mb), and ultramafic (um) schist. Kses, San Emigdio Schist; Kseg, San Emigdio gneiss; Qls, landslide deposit. Field of view ~1 km long. (f) Quartzofeldspathic veins transposed into D1 foliation. (g) Coarse quartz + feldspar melt vein. (h) Talc–actinolite lens within mafic schist. ppl, plane-polarized light; xpl, cross-polarized light.

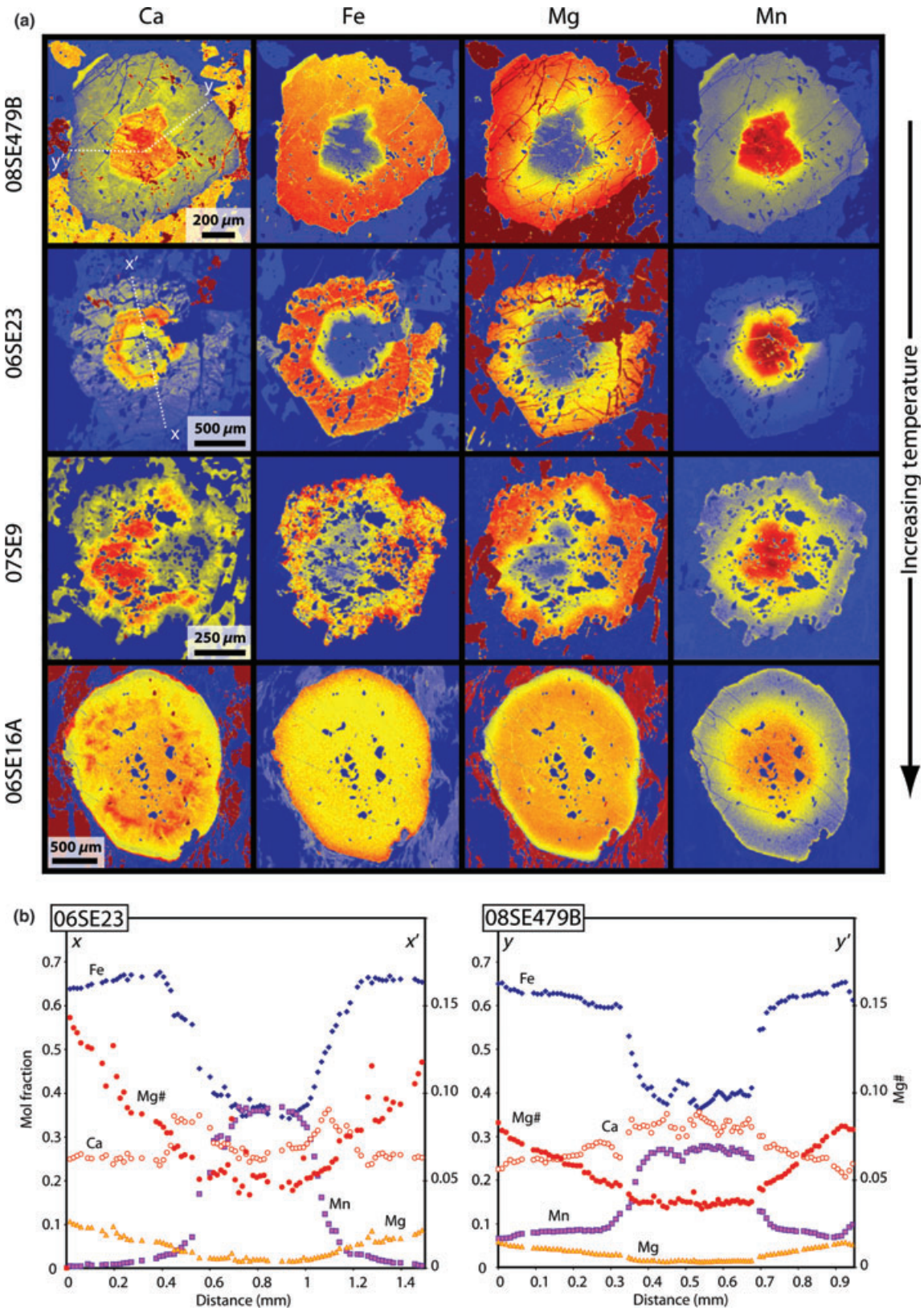

Fig. 5. (a) X-ray maps and (b) zonation profiles in schist garnet. Location of profiles shown in Ca maps of samples 06SE23 and 08SE479B. Hot colours in X-ray images represent relatively high concentration with red for the highest and bluish purple for the lowest.

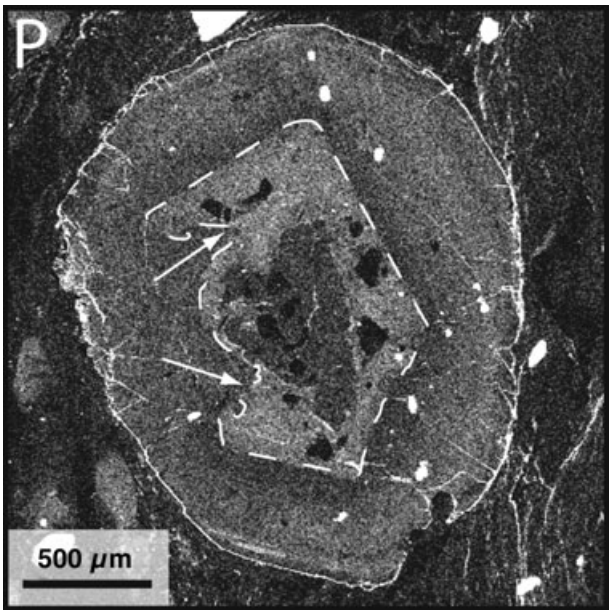

Fig. 6. X-ray map of garnet from schist sample 06SE16A for phosphorus. Note partially resorbed idioblastic core (arrows) mantled by rounded rim. Bright areas denote relatively high phosphorus.

evident in Ti X-ray maps, in the zonation pattern of broken garnet ~25 μm inward from the rims (Fig. 7). This truncation is interpreted as the original location of the broken margin. Broken garnet rims are compositionally identical to idioblastic garnet rims (cf. Figs 5 & 7) and are interpreted, based on the sharpness of the interface between juxtaposed compositions, to represent growth zonation. By this logic, overgrowth along broken margins resulted in natural diffusion couples.

Biotite, muscovite and plagioclase in metasandstone and hornblende and plagioclase in mafic schist were analysed in line traverses and X-ray maps in regions lacking D2 minerals to evaluate the extent of retrogression of the D1 assemblage. Biotite, muscovite and hornblende exhibit negligible core to rim variation in composition, while plagioclase interiors in both metasandstone and mafic varieties show patchy zonation, ranging in composition from An_{16} to An_{39} (oligoclase to andesine). Plagioclase rims are more uniform than cores, and are in apparent textural equilibrium with garnet, muscovite, biotite and quartz in metasandstones, and with garnet, hornblende, and quartz in mafic schists. We infer from these chemical and textural relationships that these assemblages were in equilibrium during peak metamorphism and are therefore suitable for thermobarometric work.

Upper plate

Garnet from the San Emigdio gneiss is almandine-rich with lesser amounts of pyrope, grossular and spessartine components (X_{alm} = 0.73–0.60, X_{prp} = 0.25–0.16, X_{grs} = 0.17–0.09 and X_{sps} = 0.04–0.01) (Fig. 8; Table S1). Representative garnet mole fractions and precision (1σ) calculated from counting statistics from sample 06SE14A are: X_{alm}, 0.627 ± 0.012; X_{grs}, 0.150 ± 0.003; X_{prp}, 0.206 ± 0.008; X_{sps}, 0.017 ± 0.002. At the scale of Fig. 8, this uncertainty is smaller than the size of the symbols representing each data point. While considerable scatter is apparent in conventional microprobe traverses, subtle variations in garnet composition are detectable within analytical uncertainty. Moreover, X-ray maps clearly resolve three distinct compositional domains in garnet from the San Emigdio gneiss. These garnet grains are generally compositionally homogeneous with flat interior profiles (zone 1) except for weak annuli in a second zone between 300 and 1500 μm from the rims (normalized distances of 0.7–0.9 from core regions). These annuli first change to relatively high concentrations of Ca, Fe and Mn, and low Mg# values, and then along the outer ~300 μm (zone 3) the trends reverse back towards interior compositions. The zone 1 mantled by zone 2 pattern is typical for garnet throughout the deep-level batholithic plate (Pickett & Saleeby, 1993), but the outermost compositional reversal is restricted to proximity to the Rand fault.

Line traverses and X-ray maps of plagioclase and hornblende porphyroblasts show little internal variation in composition, suggesting that they are not significantly modified by retrograde metamorphism. Textural relationships between garnet, hornblende, plagioclase and quartz grains in direct contact corroborate chemical evidence, outlined above, that this is an equilibrium assemblage suitable for thermobarometry.

THERMOBAROMETRY AND INVERTED METAMORPHIC FIELD GRADIENT

Equilibrium *P–T* conditions were calculated using the internally consistent average *P–T* mode in THERMOCALC, version 3.26 (Powell & Holland, 1994; Holland & Powell, 1998). Thermobarometry was done on garnet-bearing schist and upper plate samples (Fig. 9). The *P–T* conditions for metasandstone schist were calculated from garnet + plagioclase + muscovite + biotite + quartz assemblages interpreted, based on chemical and textural evidence outlined above, to have equilibrated during peak metamorphism. Garnet–hornblende thermometry and garnet–hornblende–plagioclase–quartz barometry were applied to mafic schist and upper plate lithologies. For all samples, the garnet rim compositions were used where Mg# is highest suggesting garnet growth at peak temperatures (Spear, 1993). All calculations were done assuming a water activity of unity, due to the abundance of hydrous phases. Calculated temperatures and pressures for the schist range from 590 to 700 °C and 8.5–11.1 kbar. Temperatures calculated from the San Emigdio gneiss (675–710 °C) are identical within error to those from

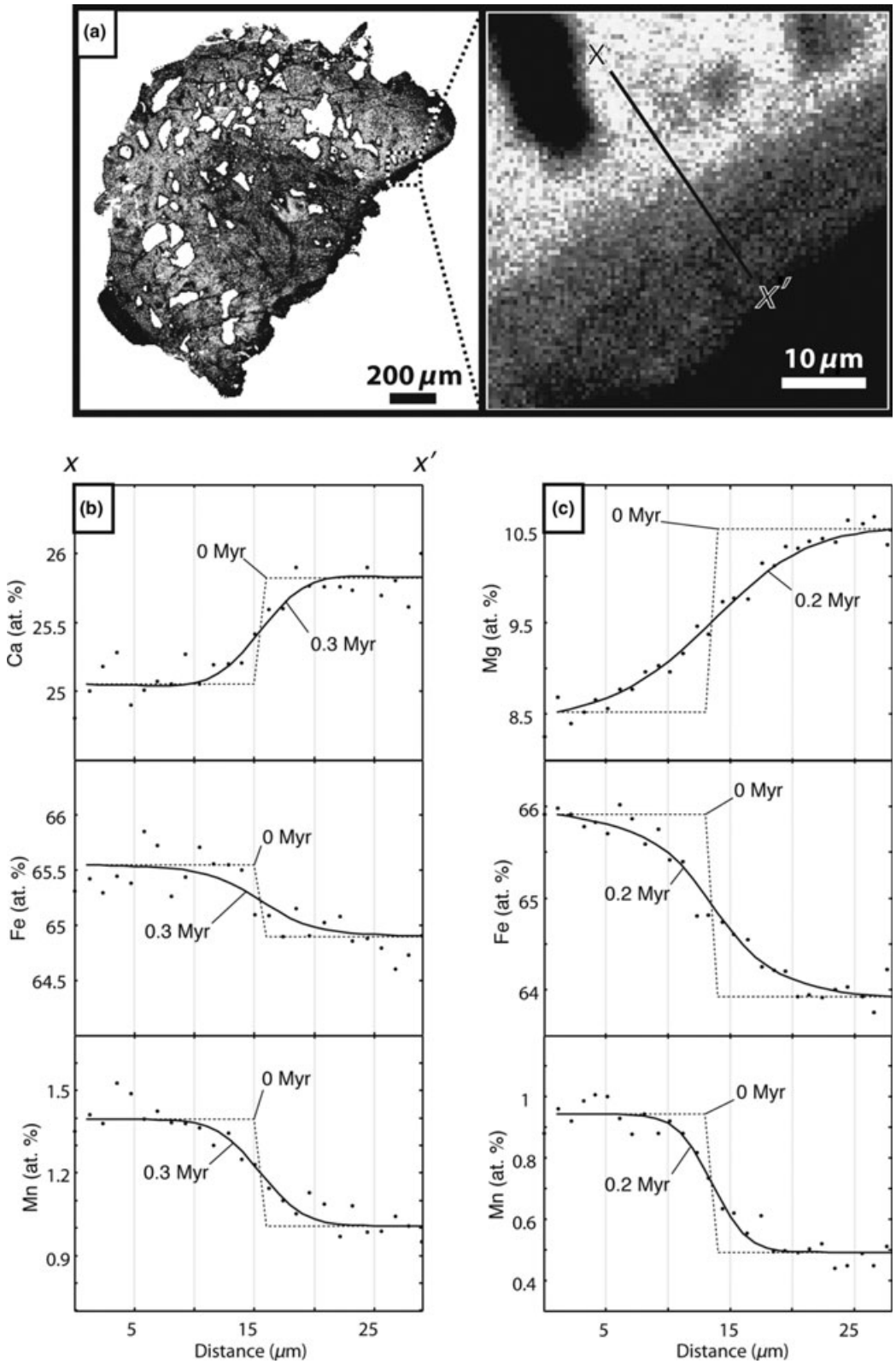

Fig. 7. (a) X-ray map of broken garnet from schist sample 06SE23 for Ti; referred to as 'grain 1' in text. (b & c) Results of diffusion modelling for grains 1 and 2, respectively. Location of profile in grain 1 shown in (a); grain 2 not shown.

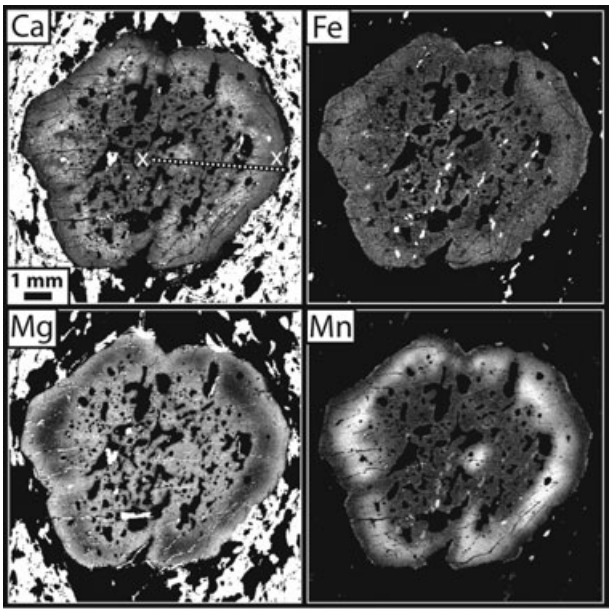

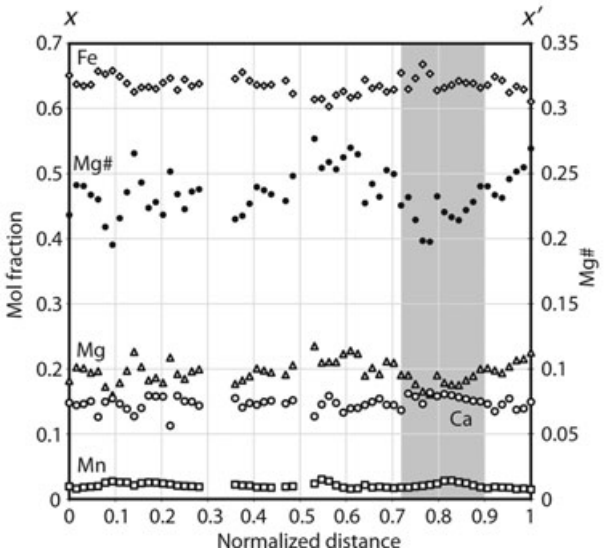

Fig. 8. (a) X-ray maps and (b) zonation profiles in garnet from upper plate sample 06SE14A. Location of profile shown in Ca map. Bright areas in X-ray images represent relatively high concentration. Garnet is ~1 cm in diameter. See text for discussion.

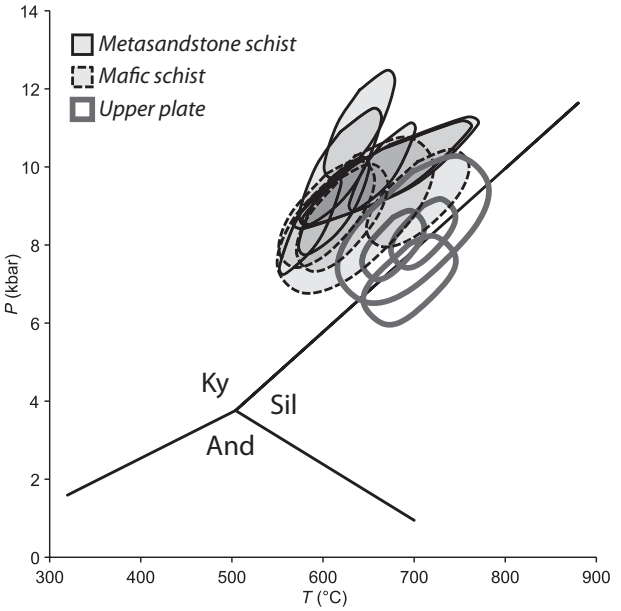

Fig. 9. Calculated pressures and temperatures for the San Emigdio Schist and upper plate San Emigdio gneiss, using THERMOCALC v. 3.26. 1σ uncertainty ellipses based on propagation of uncertainties on thermodynamic data and activity–composition relationships through thermobarometric calculations.

the uppermost levels of the schist, whereas calculated pressures are ~1 kbar lower (7.1–8.4 kbar). Results from thermobarometric work and representative mineral compositions are summarized in Tables 1 & S1–S5.

Three thermobarometric transects were done from high to low structural levels of the schist (Fig. 2). In each transect, temperature determinations from samples in close proximity to the Rand fault were ~90–120 °C higher than those from samples collected 106–1840 m below the fault. This equates to thermal gradients from 50 to 1100 °C km^{-1}. Calculated thermal gradients increase with decreasing exposed structural thickness from east to west (Fig. 2), suggesting that structural attenuation is at least partly responsible for the 1100 °C km^{-1} value. Thermal gradients of 50–240 °C km^{-1} (calculated from eastern and central transects, respectively) are similar to those reported in the schist of Sierra de Salinas (50–70 °C; Kidder & Ducea, 2006) and in the Pelona Schist (240 °C km^{-1}; Graham & Powell, 1984).

THERMODYNAMIC MODELLING AND *P–T* PATHS

Prograde garnet zonation features in the schist are remarkably well-preserved, allowing for straightforward recovery of a large portion of the early *P–T* history of the schist. The *P–T* paths for metasandstone and mafic schist samples were constrained using petrography, garnet zonation patterns and *P–T* pseudosection calculations. A description of the thermodynamic modelling routine is given in Appendix S1. Figure 10a shows a *P–T* pseudosection for the bulk composition of sample 06SE23. The peak mineral assemblage garnet + plagioclase + muscovite + biotite + quartz present in 06SE23 is quite common in other metasandstones from intermediate to high structural levels of the schist and is consistent with those predicted from the pseudosection. The *P–T* results from THERMOCALC plot within the field of the peak assemblage and are in close proximity to the H_2O-saturated solidus.

Table 1. Summary of thermobarometric calculations from the San Emigdio Mountains.

Sample	Lithology	UTM easting[a]	UTM northing[a]	Distance to Rand fault (m)[b]	Mineralogy	T (°C)[c]	P (kbar)[c]	Corr.[d]
08SE202	Upper plate	322237	3863252	357	Grt Hbl Pl Qz	695 ± 40	7.1 ± 0.9	0.555
08SE270	Upper plate	309137	3861143	3	Grt Hbl Pl Qz	699 ± 66	8.4 ± 1.5	0.604
04SE1a	Upper plate	310571	3861983	0	Grt Hbl Pl Qz	710 ± 28	8.3 ± 0.7	0.577
06SE14a	Upper plate	310573	3861982	0	Grt Hbl Pl Qz	677 ± 27	8.0 ± 0.7	0.586
08SE467[e]	Metasandstone	319332	3864641	0	Grt Bt[f]	>700	ND	NA
06SE16a[e]	Metasandstone	310569	3861996	0	Grt Bt[f]	>700	ND	NA
06SE74a	Metabasalt	311043	3861862	0	Grt Hbl Pl Qz	704 ± 45	9.2 ± 1.0	0.661
07SE17	Metasandstone	316031	3863579	−5	Grt Ms Bt Pl Qz	665 ± 78	9.8 ± 1.1	0.879
06SE23	Metasandstone	310593	3861943	−30	Grt Ms Bt Pl Qz	665 ± 29	10.0 ± 0.9	0.845
06SE54	Metasandstone	310682	3861857	−60	Grt Ms Bt Pl Qz	619 ± 36	10.0 ± 1.2	0.800
06SE9	Metasandstone	310713	3861775	−106	Grt Hbl Ms Bt Pl Qz	586 ± 27	8.5 ± 1.0	0.844
07SE19	Metasandstone	316248	3863358	−229	Grt Ms Bt Pl Qz	612 ± 31	9.0 ± 1.0	0.783
08SE469	Metasandstone	319291	3864057	−254	Grt Ms Bt Pl Qz	674 ± 77	9.9 ± 1.1	0.870
08SE478[g]	Metasandstone	321131	3861596	−1250	Grt Bt Pl Qz	619 ± 77	10.0	NA
08SE474	Metabasalt	320041	3862435	−1368	Grt Hbl Pl Qz	604 ± 42	8.8 ± 1.1	0.661
08SE475	Metabasalt	320182	3862264	−1434	Grt Hbl Pl Qz	621 ± 40	8.7 ± 1.1	0.650
08SE479b	Metabasalt	320620	3862026	−1545	Grt Hbl Pl Qz	633 ± 66	8.7 ± 1.6	0.662
08SE476	Metasandstone	321804	3860814	−1840	Grt Ms Bt Pl Qz	640 ± 31	11.1 ± 1.1	0.776

ND, not determined; NA, not applicable.
[a]UTM coordinates are WGS datum, zone 11N.
[b]Distance to Rand fault: positive and negative values indicate position above and below the Rand fault, respectively.
[c]1σ uncertainties based on propagation of uncertainties on thermodynamic data and activity–composition relationships through thermobarometric calculations.
[d]Correlation coefficient between pressure and temperature from THERMOCALC.
[e]Sample shows evidence of partial melt.
[f]Phases not touching; lack of primary muscovite and presence of partial melt suggests >700 °C at 10 kbar (Fig. 10a), assuming similar bulk composition to 06SE23.
[g]Garnet–biotite temperatures; calculated at 10 kbar.

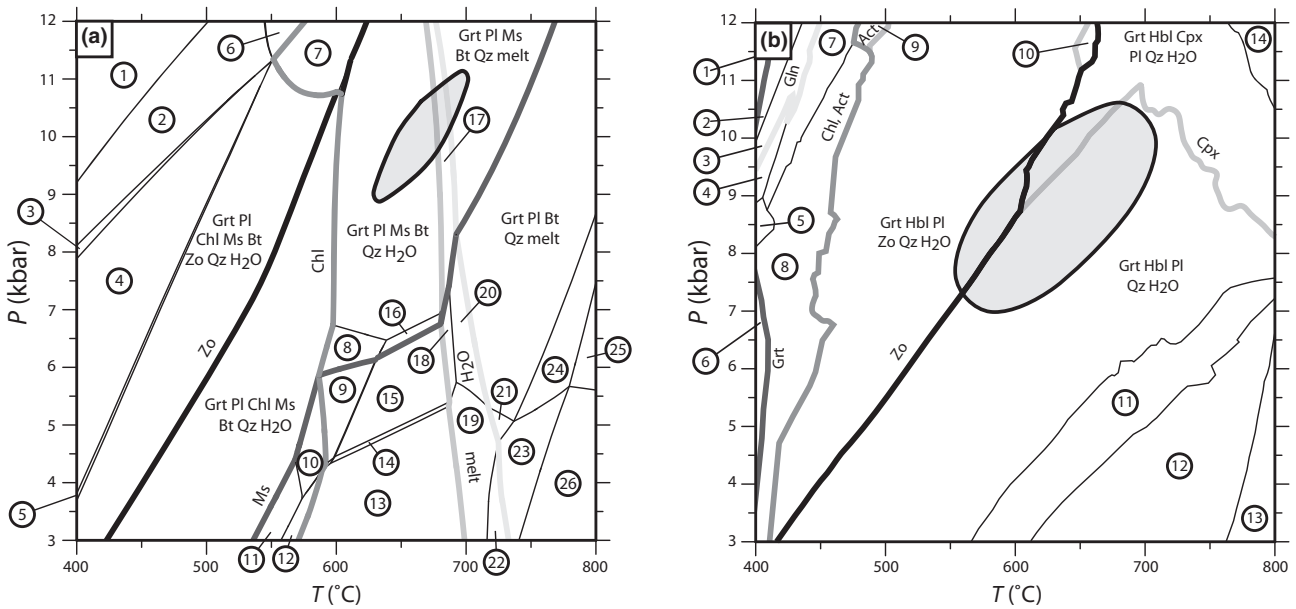

Fig. 10. Calculated 'prograde' P–T pseudosections for samples (a) 06SE23 and (b) 08SE479B. THERMOCALC results overlain for comparison. Numbered fields listed in Appendix S2. Bulk compositions listed in Table S6.

Figure 11 shows the pseudosection of Fig. 10a superimposed with volume per cent H_2O in solids, garnet abundance contours, and almandine, spessartine, grossular and pyrope isopleths. In general, X_{alm} and X_{prp} are strongly temperature-dependent, X_{sps} is strongly pressure-dependent, and at high temperatures X_{grs} is as pressure-dependent as X_{sps}. We calculate conditions of garnet nucleation from the intersection of end-member isopleths that correspond to garnet core compositions (e.g. Vance & Mahar, 1998). The intersection of the garnet core composition isopleths (X_{alm} = 0.35, X_{sps} = 0.37, X_{grs} = 0.26 and X_{prp} = 0.02) indicates the temperature and pressure conditions at the onset of growth. Although garnet contains no inclusions useful for thermobarometry, which prohibits an independent check of the conditions of garnet core formation, the tight intersection of the compositional contours at the point 4.3 kbar, 475 °C strongly

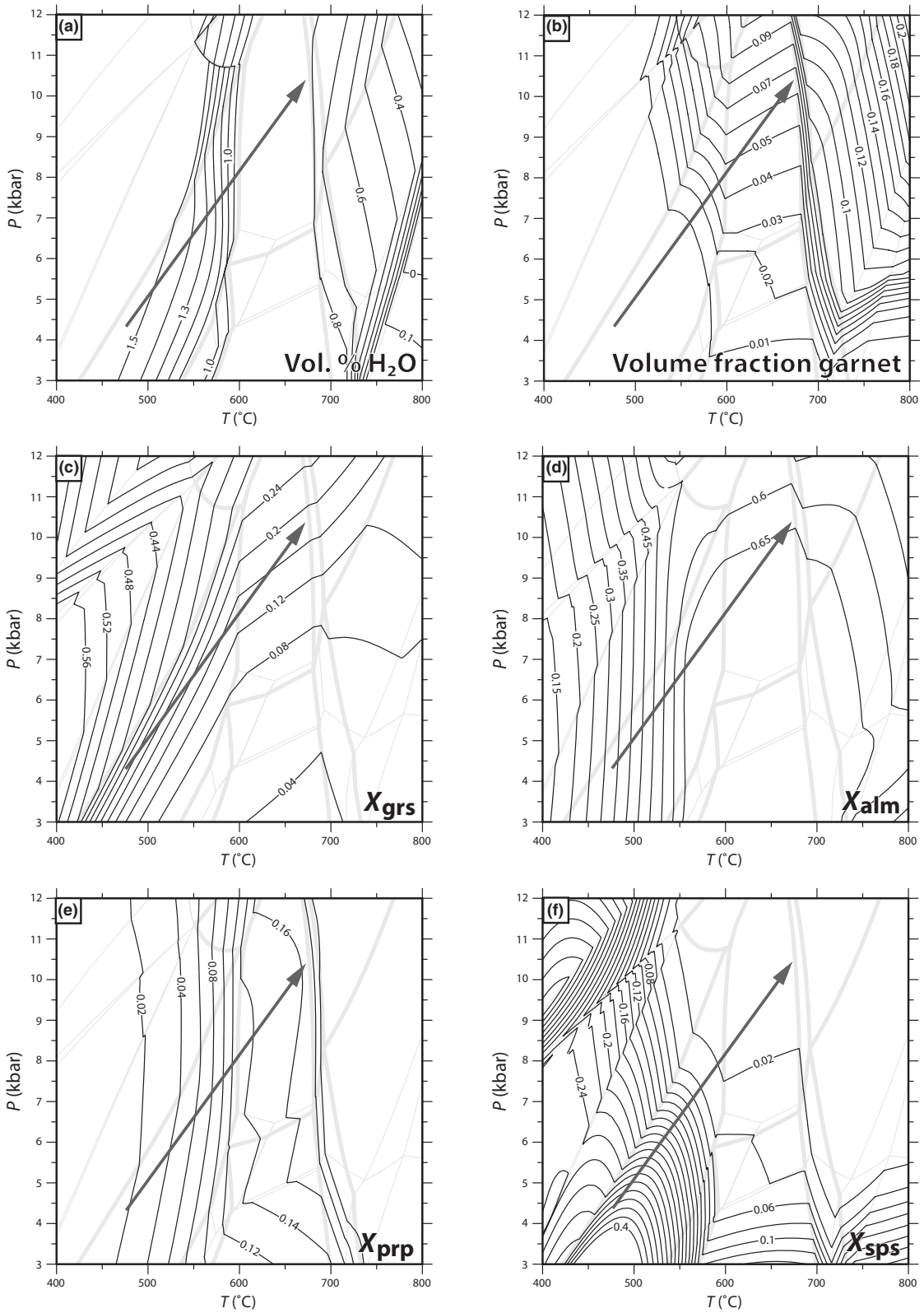

Fig. 11. Pseudosection shown in Fig. 10a with contours of (a) volume per cent H_2O in solids, (b) volume fraction garnet and (c–f) garnet composition expressed as mol fractions overlain. Arrow represents inferred prograde *P–T* trajectory.

suggests that the pseudosection accurately reproduces the physical conditions of garnet nucleation.

Mafic sample 08SE479b contains the peak assemblage garnet + plagioclase + hornblende + quartz and is representative of mafic schist outcrops >100 m from the Rand fault. The pseudosection of Fig. 10b is overlain by garnet isopleths in Fig. 12. Garnet core composition isopleths (X_{alm} = 0.36, X_{grs} = 0.35, X_{sps} = 0.28 and X_{prp} = 0.02) intersect at ~6.5 kbar, 575 °C. Mineral isopleth-based constraints of garnet nucleation in both metasandstone and mafic schist lie well inside the stability field of garnet as predicted by equilibrium growth (Figs 10–12). This is most likely due to the effect of missing Mn end-members in the solution models of competing phases. The presence of Mn-bearing chlorite, biotite and ilmenite during prograde metamorphism would hinder garnet nucleation and growth at low metamorphic grades, restricting its stability field to higher pressures and temperatures. Additional explanations for this observation include: (i) late metastable nucleation of garnet (i.e. overstepping of the garnet isograd), (ii) limited local equilibrium due to slow reaction kinetics at low temperatures, and (iii) diffusional modification of the core.

Prograde paths for garnet in samples 06SE23 and 08SE479b are approximated by interpolating the conditions of garnet core formation with peak metamorphic conditions. The preferred prograde paths outlined in Figs 11 & 12 incorporate these constraints and take into consideration: (i) the lack of prograde clinozoisite in sample 06SE23 and the presence of prograde epidote in sample 08SE479b; (ii) the preservation of primary muscovite in sample 06SE23; and (iii) the lack of evidence for partial melting in these samples, although such evidence is present at higher structural levels in the schist. Therefore, the likely prograde path for sample 06SE23 involves burial from ~4.3 to 10 kbar and contemporaneous heating from 475 to 665 °C. Along this path, the only net transfer reaction encountered in sample 06SE23 during garnet growth is the chlorite-out reaction. The lack of primary chlorite as inclusions within garnet probably resulted from garnet scavenging Fe, Mg, Al and Si from the mineral, which was likely present during garnet core growth. The prograde trajectory of sample 08SE479b overlaps that of 06SE23, with conditions increasing from 7 kbar, 575 °C to 8.4 kbar, 636 °C. It is important to note that although the preferred prograde *P–T* paths shown in Figs 11 & 12 explain many core-to-rim garnet zonation trends in samples 06SE23 and 08SE479b (e.g. monotonically increasing X_{prp}, monotonically decreasing X_{sps}, approximately constant X_{grs} and increasing X_{alm} prior to reaching a compositional plateau in the outer 400 μm), modelled garnet isopleths do not match the composition of garnet beyond the cores at any point in *P–T* space. In other words, the garnet core compositions are the only regions that can be successfully modelled. This is because the assumption of equilibrium garnet growth is no longer valid outside the cores. Isopleth intersection thermobarometry breaks down following garnet core growth because the bulk rock composition is changed as garnet sequesters material, particularly Mn, forever removing it from the system unless the temperature becomes sufficiently high that diffusion and/or resorption reintroduces it to the system (Spear, 1993; Vance & Mahar, 1998). Figure 13 compares modelled and observed garnet zonation patterns and illustrates the effect of fractional crystallization for the preferred prograde path of sample 06SE23 (see Appendix S1 for a description of the calculation routine). This effect is to deplete the bulk rock composition, leading to a decrease in nutrient availability at the garnet surface and a corresponding decrease in growth rate. While the observed garnet zonation is fit quite well by the equilibrium growth model, some proportion of fractional crystallization may explain sharp compositional gradients in the San Emigdio Schist garnet, particularly in Mn. While we do not consider the effect of volume diffusion in garnet, some amount of diffusional relaxation of these steep compositional variations has probably occurred. High-Ca annuli in garnet from metasandstone schist (Figs 5 & 13) cannot be explained by fractional crystallization alone and probably reflect chemical disequilibrium during prograde metamorphism (Chernoff & Carlson, 1999; Konrad-Schmolke *et al.*, 2005; Chapman *et al.*, 2006).

Zonation preserved in garnet from samples 06SE23 and 08SE479b indicates that growth did not occur under decreasing pressure and/or temperature conditions (i.e. following peak conditions). Contours of garnet volume per cent are generally nearly isothermal with slightly negative slopes, indicating that it is impossible to grow garnet during decompression in these bulk compositions. Furthermore, garnet rims are characterized by decreasing X_{alm} and X_{sps} and increasing X_{prp}, which is only possible under conditions of increasing temperature (Figs 11 & 12).

The prograde path described above involves dehydration reactions, fluid loss (Figs 11a & 12a), and sequestration of Al, Ca, Fe, Mg, Mn and Si associated with garnet fractionation. In addition, peak assemblages are well-preserved, indicating that the necessary H_2O was not available to promote extensive retrogression. However, free water must have been locally present to stabilize the D2 assemblage. Therefore, to reconstruct the retrograde path of the schist, separate pseudosections were drawn for the bulk compositions of samples 06SE23 and 08SE479B with sufficient free water (i.e. water-saturated) to stabilize chlorite and clinozoisite along the retrograde path (Fig. 14). For simplicity, it is assumed that the bulk composition effectively equilibrating during retrogression is similar to the original bulk composition from which garnet was subtracted (garnet rims preserve peak *P–T* composition and show no retrogressive modification). We estimated the modal proportion of garnet,

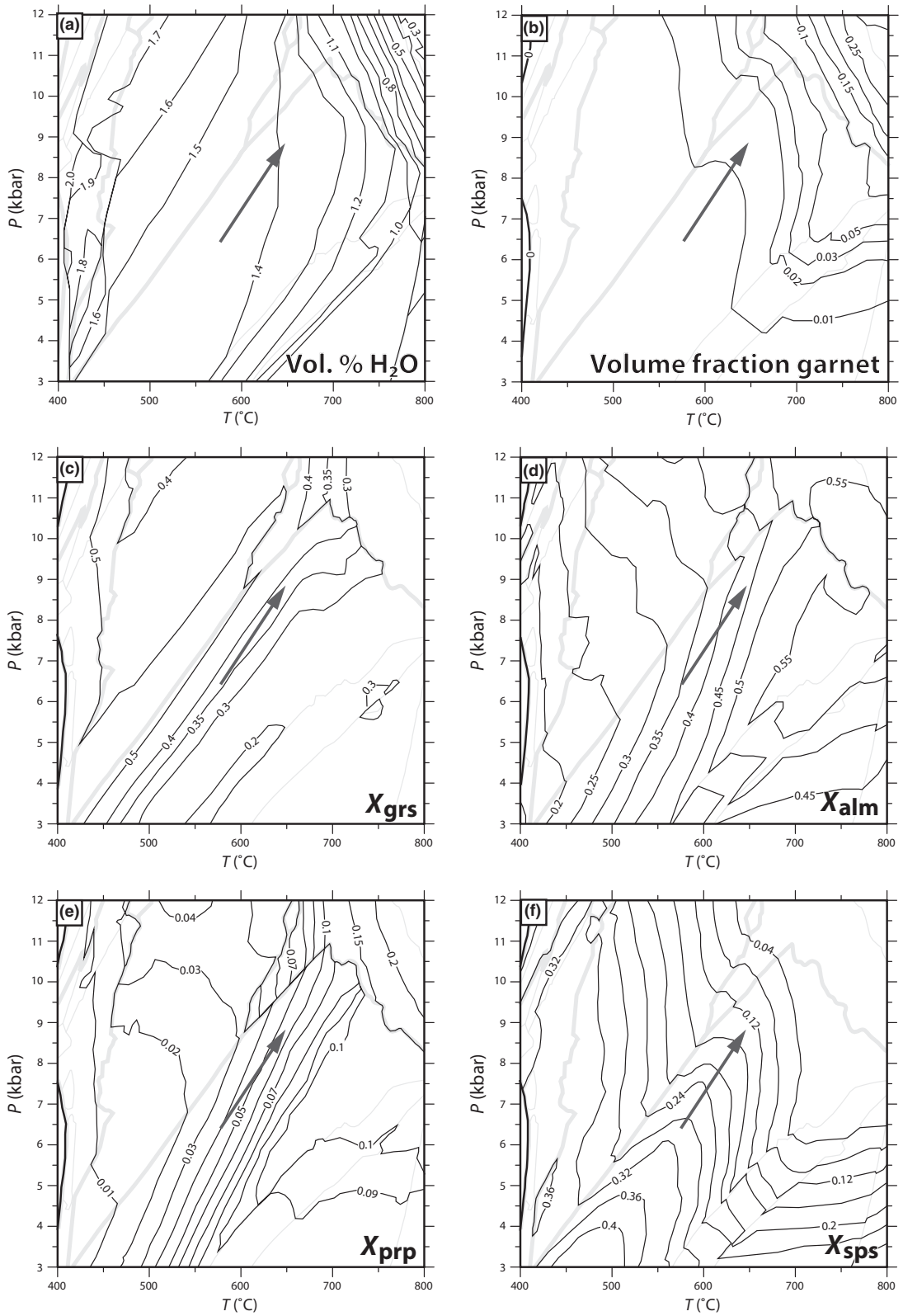

Fig. 12. Pseudosection shown in Fig. 10b with contours of (a) volume per cent H_2O in solids, (b) volume fraction garnet and (c–f) garnet composition expressed as mol fractions overlain. Arrow represents inferred prograde *P–T* trajectory.

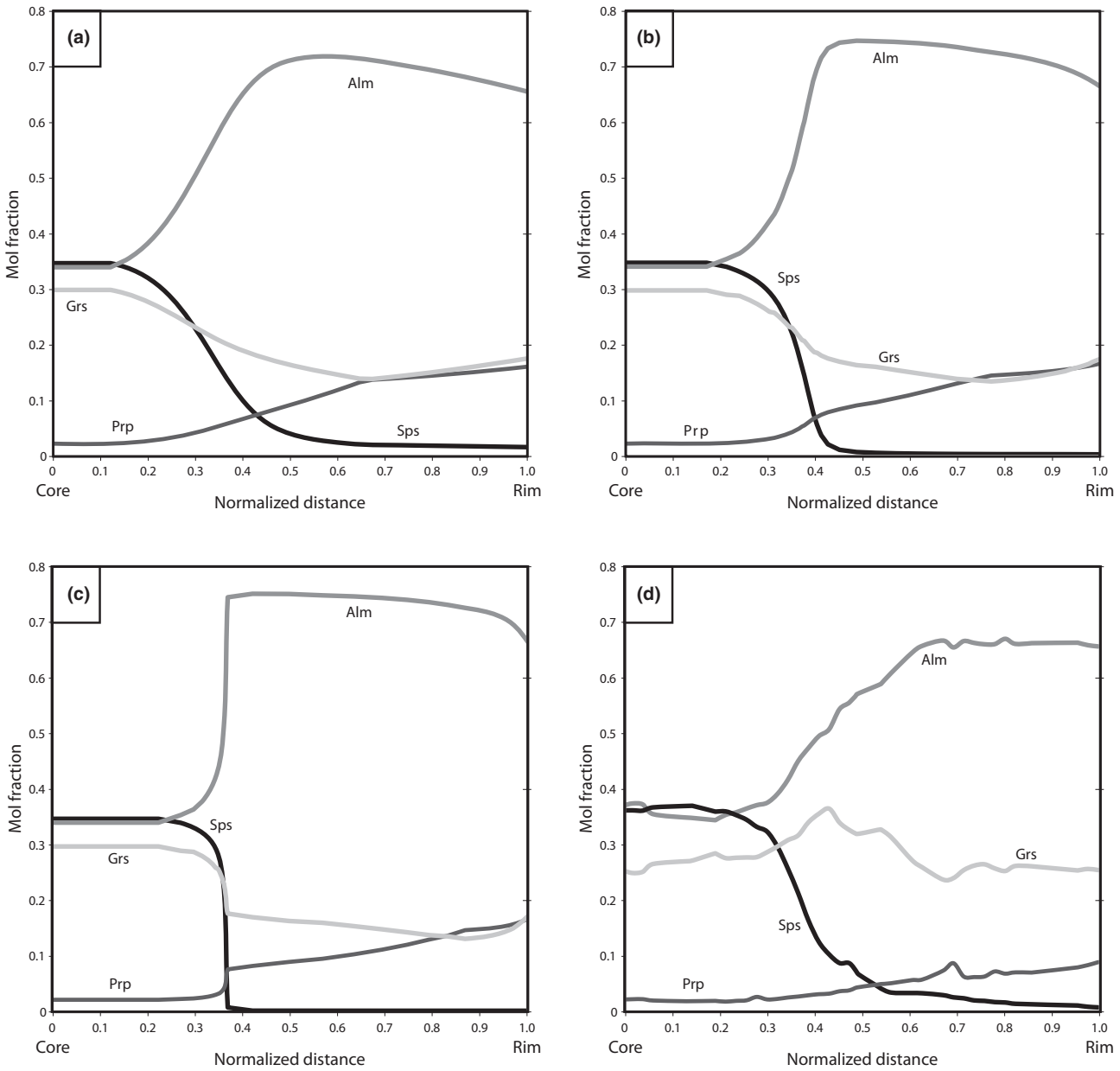

Fig. 13. Comparison of modelled garnet zonation patterns (a–c) and observed garnet compositional profiles (d). Modelled profiles for the prograde *P–T* trajectory shown in Fig. 11 (sample 06SE23) for (a) homogeneous equilibrium crystallization, (b) 10% fractional crystallization and (c) 25% fractional crystallization.

approximated the composition of garnet grains by subdividing them into constituent zones and adding together the contribution of each zone, and finally calculated and subtracted the contribution of garnet to the bulk compositions.

The retrograde paths outlined in Fig. 15 are based on the stabilization of D2 assemblages. As garnet growth ceased and metasandstone schist (06SE23) entered the retrograde portion of the *P–T* path, chlorite and clinozoisite were stabilized. According to the retrograde pseudosection for sample 06SE23, this sample must have followed a trajectory with similar *P–T* slope during decompression than during burial to pass through the stability fields of chlorite and clinozoisite. Although epidote entered the stable mineral assemblage in mafic schist (08SE479b) varieties following peak metamorphism, chlorite and actinolite stability fields were not traversed along the retrograde path. The pseudosection for sample 08SE479b indicates that this is possible if the retrograde *P–T* trajectory passed between the chlorite/actinolite-out and clinozoisite/epidote-out reaction boundaries.

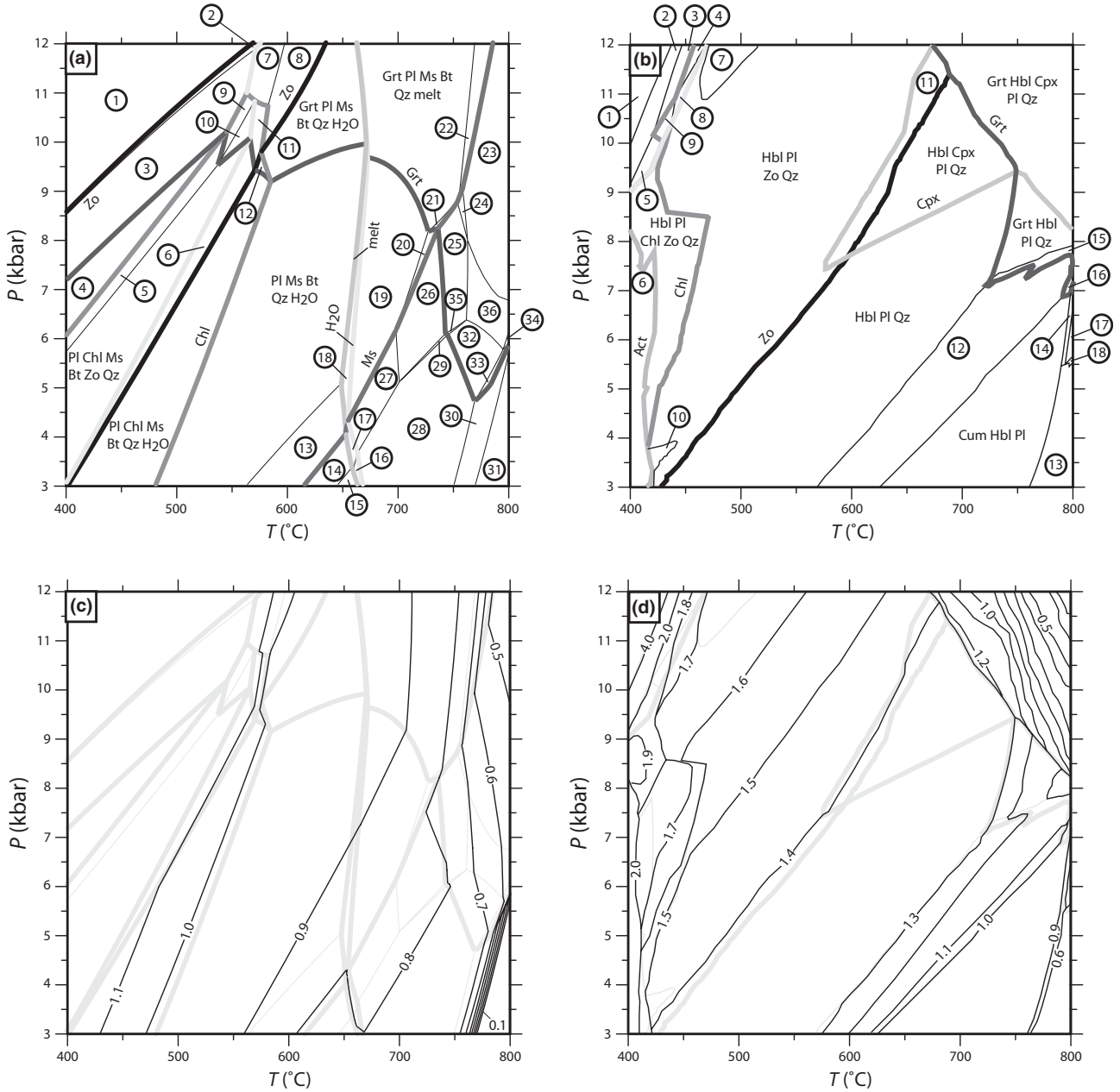

Fig. 14. Calculated 'retrograde' *P–T* pseudosections for samples (a) 06SE23 and (b) 08SE479B with (c & d) contours of volume per cent H_2O in solids overlain. Numbered fields listed in Appendix S2. Bulk compositions listed in Table S6.

Figure 15 shows, for both metasandstone and mafic schist, two end-member retrograde paths that satisfy the constraints outlined above: (i) one with a shallower *P–T* slope than the prograde path (i.e. a counter-clockwise *P–T* loop) and (ii) one with a steeper slope (i.e. a clockwise *P–T* loop). While the retrograde path cannot be further constrained, we consider it likely that the geometry of the *P–T* loop for the schist lies between the end-member possibilities with roughly overlapping prograde and retrograde *P–T* trajectories (i.e. 'Franciscan-type' or 'out and back' *P–T* path; Ernst, 1988).

The retrograde paths shown in Fig. 15 involve the formation of clinozoisite/epidote and/or chlorite, which require the presence of H_2O to take place. Along these retrograde paths, each sample encounters contours of increasing H_2O content, implying that the assemblage becomes fluid-absent unless fluid is available along grain boundaries or is externally derived (Fig. 14) (Guiraud *et al.*, 2001). Therefore, overprinting of peak assemblages by D2 minerals is evidence for open system behaviour involving H_2O influx.

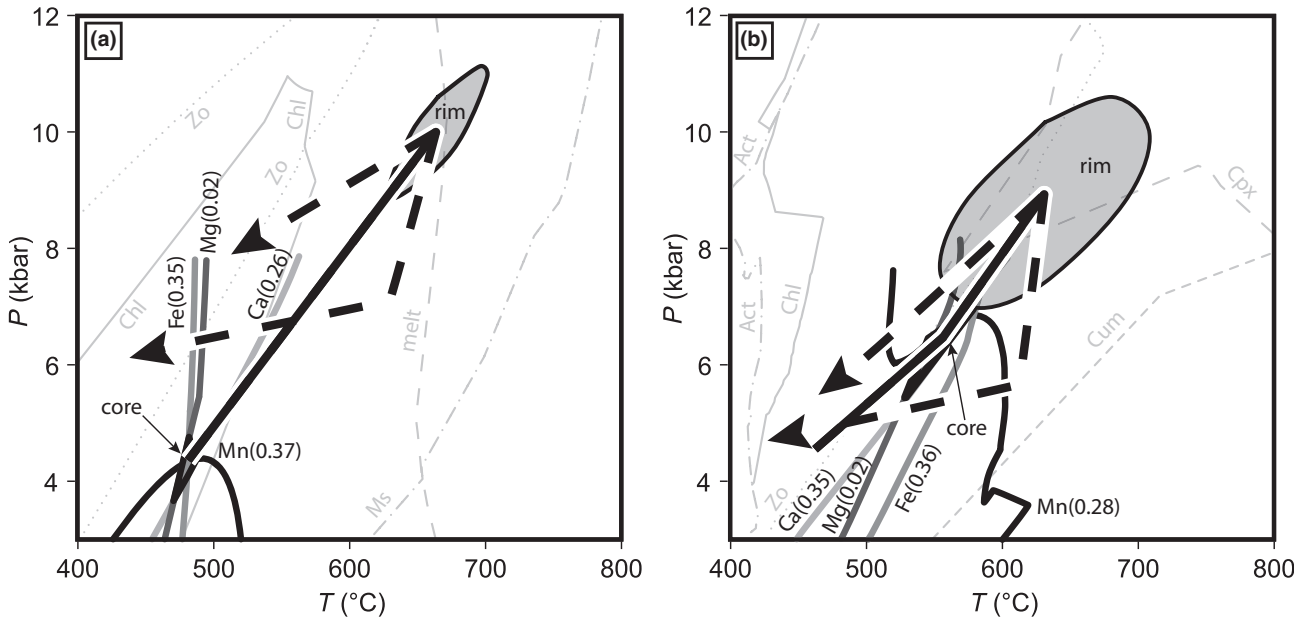

Fig. 15. *P–T* evolution for samples (a) 06SE23 and (b) 08SE479B. Prograde paths shown as solid lines. (a) 'Core' conditions from intersection of garnet isopleths in Fig. 11, 'rim' conditions from Fig. 9, end-member retrograde paths (dashed lines) constrained by the stability of chlorite and clinozoisite (fields from Fig. 14a). (b) 'Core' conditions from intersection of garnet isopleths in Fig. 12, 'rim' conditions from Fig. 9, end-member retrograde paths (dashed lines) constrained by the stability of clinozoisite and the lack of retrograde chlorite (fields from Fig. 14b).

DIFFUSION MODELLING OF BROKEN GARNET

Sample 06SE23 contains two garnet grains that ruptured and subsequently overgrew their broken margins, creating sharp compositional discontinuities. When a mineral overgrows itself in this fashion, the resulting interface between juxtaposed compositions in the composite grain is a natural diffusion couple. The degree of relaxation of the originally steep compositional step is dependent chiefly on temperature and the time interval over which diffusion was possible.

We exploit the diffusional annealing of the hypothetically originally sharp compositional steps in broken garnet from sample 06SE23 to estimate the amount of time required for their relaxation. It is assumed that the amount of time required for overgrowth of broken garnet margins is infinitesimally small compared to the rates of diffusion (Ganguly *et al.*, 1996; Dachs & Proyer, 2002). The diffusive time-scales for two grains in sample 06SE23 are modelled. For grain 1, Ca, Fe and Mn profiles, and for grain 2, Fe, Mg and Mn profiles were modelled. We did not attempt to model Mg and Ca in grains 1 and 2, respectively, due to the erratic nature of the measured profiles.

The analytical program PROFILER (available in Glicksman, 2000) was used to calculate interdiffusion coefficients and time-scales of diffusion from measured compositional profiles. PROFILER solves Fick's second law for multicomponent diffusion couples based on user specified end-member compositions, distance, temperature, pressure, diffusion time-scale and self-diffusion data. The solutions calculated from PROFILER are only valid if diffusion coefficients do not vary with time. As diffusion coefficients are not constant during non-isothermal processes, such as during progressive metamorphism, Chakraborty & Ganguly (1991, 1992) developed the concept of a 'characteristic temperature', T_{ch}, which yields identical diffusive relaxation profiles when compared with those of metamorphic *T–t* paths. The San Emigdio Schist certainly experienced non-isothermal metamorphism during underplating and exhumation, and as such, the relationship $T_{ch} \approx 0.97T_{peak}$ was used to calculate characteristic temperatures based on peak metamorphic temperature estimates from thermobarometry. A discussion of model parameters and the theory behind garnet diffusion modelling is given in Appendix S1.

Garnet end-member compositions achieve plateau values adjacent to the diffusion zone in both grains (Fig. 7). Interdiffusion coefficients were calculated for each profile using thermobarometric constraints on sample 06SE23 (Table 1) at 10 kbar and $T_{ch} \approx 0.97T_{peak} = 645$ °C. In each case, the relaxation time was adjusted until modelled results could be visually fit to analytical profiles. Diffusion time-scales of 0.3 and 0.2 Myr were calculated from grains 1 and 2, respectively (Fig. 7). These values represent the amount of time required to cool garnet from peak temperatures to ~500–550 °C, below which garnet compositions

become locked in due to sluggish diffusion kinetics (Ganguly, 2002). Therefore, garnet from sample 06SE23 cooled from peak conditions at rates between 825 and 380 °C Myr^{-1}.

Deformation proceeded following the cessation of garnet growth into the stability field of D2 minerals. Morphologically similar broken garnet from deeper structural levels did not overgrow the broken margins and therefore, may have broken following peak conditions (Fig. 4).

DISCUSSION

Inverted metamorphism

The presence of an inverted metamorphic field gradient in the San Emigdio Schist, i.e. an upsection increase in peak temperature, is a characteristic feature of this and the majority of other southern California schist exposures (e.g. Ehlig, 1981; Sharry, 1981; Graham & Powell, 1984; Jacobson, 1995; Kidder & Ducea, 2006). Our petrological and thermobarometric work indicate that the San Emigdio Schist exhibits a gradation from upper amphibolite facies (~700 °C) to epidote–amphibolite facies (~600 °C) with increasing structural depth. We resolve no clear relationship between calculated metamorphic pressures and structural depth. Inverted temperature gradients preserved in other exposures of the southern California schist have been explained by: (i) shear heating along the subduction interface (Graham & England, 1976; England & Molnar, 1993; Ducea *et al*., 2009), (ii) rapid *en masse* underthrusting of cold schist beneath a hot upper plate (i.e. the 'hot iron effect', Peacock, 1992), and (iii) tectonic underplating and progressive cooling beneath an initially hot upper plate following the onset of shallow subduction (Peacock, 1992; Kidder & Ducea, 2006). Each scenario requires rapid cooling to preserve the inverted gradient. Explanations 1 and 2 require that the metamorphic gradient preserved in the schist records a geothermal gradient that existed during subduction, while scenario 3 does not. Although our results do not cast new light on this long-standing debate, we believe that scenario 3 provides the most satisfactory explanation of inverted metamorphism in the schist for the following reasons:

1. To preserve the inverted gradient in scenario 1, the effect of shear heating must become less significant following schist accretion to the upper plate. This may be accomplished through cessation or slowing of subduction, for which there is no evidence, or by re-localization of the megathrust beneath the schist–upper plate contact.
2. The schist was too weak to have experienced any significant shear heating. Kidder & Ducea (2006) argued, based primarily on evidence of partial melting and ductile deformation of quartz, that the schist is incapable of supporting shear stresses of 50–90 MPa required by the shear heating hypothesis.
3. The upper plate was hot, with peak temperatures of 680–790 °C in the TSE complex (Pickett & Saleeby, 1993; this study). Kidder & Ducea (2006) argued, based on a one-dimensional thermal model, that high temperatures exhibited in upper levels of the schist (~700 °C) can be reached in ~0.3 Myr when exposed to an upper plate at 800 °C.
4. Scenario 2 requires subduction of the entire schist section as a single tectonic slice. While no major internal structural breaks have been identified in the schist, synchronous formation of the entire schist section is an unlikely scenario given that inverted metamorphic gradients rarely represent fossilized thermal gradients (e.g. Jamieson *et al*., 1996).

Metamorphic convergence between upper and lower plates

In the San Emigdio Mountains, the schist and upper plate share similar structural relations and mineral parageneses. For instance, temperature estimates from the top of the schist and the base of the upper plate are identical within error (665–710 °C) and foliations and lineations in the schist are parallel to those in the upper plate and intervening mylonites (Chapman *et al*., 2010). Similar criteria were used by Ehlig (1981) and later by Jacobson (1997) to identify the Vincent fault, an ~1-km-thick shear zone separating the Pelona Schist from superjacent upper plate rocks, as an intact remnant of the Cretaceous megathrust. However, Rand fault mylonites in the San Emigdio Mountains are clearly associated with retrograde metamorphism and indicate top to the east (i.e. trench-directed) shear (Chapman *et al*., 2010). Therefore, we view metamorphic convergence between upper and lower plates in the San Emigdio Mountains as a structural coincidence. During shallow subduction, the schist must have been carried ~150 km inboard to reach a depth of 30 km (9 kbar) (Kidder & Ducea, 2006). We suggest that the schist came in contact with a hot (~800 °C) upper plate at these conditions, whereas the upper plate rocks that the schist would later come in contact with had already decompressed from 9 to 4 kbar conditions (Saleeby *et al*., 2007). In other words, we view the schist–upper plate contact preserved in the San Emigdio Mountains as being proximal to the original subduction megathrust, but subsequent schist ascent would have placed the hot schist against an upper plate that had already experienced significant cooling during uplift from deep levels (Fig. 16).

Thermochronometric studies of the upper plate indicate that within ~100 m of the Rand fault, biotite Ar/Ar and Rb/Sr as well as (U–Th)/He zircon systems were reset as a consequence of schist ascent (Saleeby *et al*., 2007). Hornblende Ar/Ar systems were only affected in pervasively mylonitized rocks along the basal aureole of the upper plate. Such reheating by the schist is also recorded in proximal upper plate garnet compositional profiles. Compositionally flat garnet interiors (zone 1) with increasing

X_{grs}, X_{alm} and X_{sps} and decreasing X_{prp} and Mg# at the rim (zone 2) are typical of garnet throughout the TSE complex (Pickett & Saleeby, 1993). In the San Emigdio gneiss, however, an additional zone (zone 3) overgrows zone 2 with compositions similar to those found in zone 1. In aggregate, we interpret the San Emigdio gneiss garnet patterns to indicate deep-crustal residence at elevated temperatures (zone 1), followed by cooling (zone 2), and reheating (zone 3) of the base of the upper plate adjacent to the ascending schist along the Rand fault.

P–T path

The schist of the San Emigdio Mountains has likely undergone a 'Franciscan-type' *P–T* path. Thermal models of subduction initiation (Cloos, 1982, 1985; Peacock, 1987; Kincaid & Sacks, 1997; Gerya *et al.*, 2002) demonstrate high geothermal gradients (between a hot upper plate and cool lower plate) that relax with continued subduction as the upper plate cools. A possible explanation for our calculated *P–T* trajectories is in a newly initiated subduction zone with a decreasing geothermal gradient. Subduction of a conjugate massif to the Shatsky Rise is hypothesized to have driven slab flattening, thereby removing the mantle wedge and lowermost crust and repositioning the subduction zone along mid-to lower crustal levels of the recently active Late Cretaceous arc (Saleeby, 2003; Ducea *et al.*, 2009). Later schist underplating led to refrigeration of the upper plate and relaxation of the initially high geothermal gradient. Similar scenarios are envisioned to explain *P–T* trajectories calculated from high-grade blocks in the Franciscan Complex (e.g. Wakabayashi, 1990; Krogh *et al.*, 1994), eclogites in the Yukon–Tanana terrane (Perchuk *et al.*, 1999), and in the subduction-related migmatitic Sierra del Convento mélange (Garcia-Casco *et al.*, 2008). Following peak conditions, the subducted schist ascended by trench-directed channelized extrusion (Chapman *et al.*, 2010). This stage is recorded by the stabilization of D2 minerals in metasandstone and mafic schist samples as the schist cooled rapidly (between 825 and 380 °C Myr^{-1}) from peak conditions. As prograde and retrograde portions of the *P–T* path shown in Fig. 15 follow similar trajectories, retrograde alteration of peak assemblages is limited. As a result, D1 assemblages are remarkably well preserved, as is commonly the case for the Franciscan Complex (Spear, 1993). Rapid cooling during decompression may also explain well-preserved garnet zonation features and the lack of 'Mn kick-ups' except at high structural levels.

Prograde elevated stresses and strain rates and rapid cooling following peak conditions

Garnet is a high-strength mineral, with high yield stress (~7 GPa; Pardavi-Horváth, 1984), Peierls stress (resistance to dislocation glide) (Karato *et al.*, 1995) and toughness (resistance to fracture) (Whitney *et al.*, 2007). Therefore, brittle deformation of natural garnet during metamorphism, while incompletely understood (Whitney, 1996), is probably restricted to very high stresses and strain rates. Broken garnet from the San Emigdio Schist exhibits similar microstructures to brittlely deformed garnet from the Sesia Zone of the Western Alps, which are attributed to major

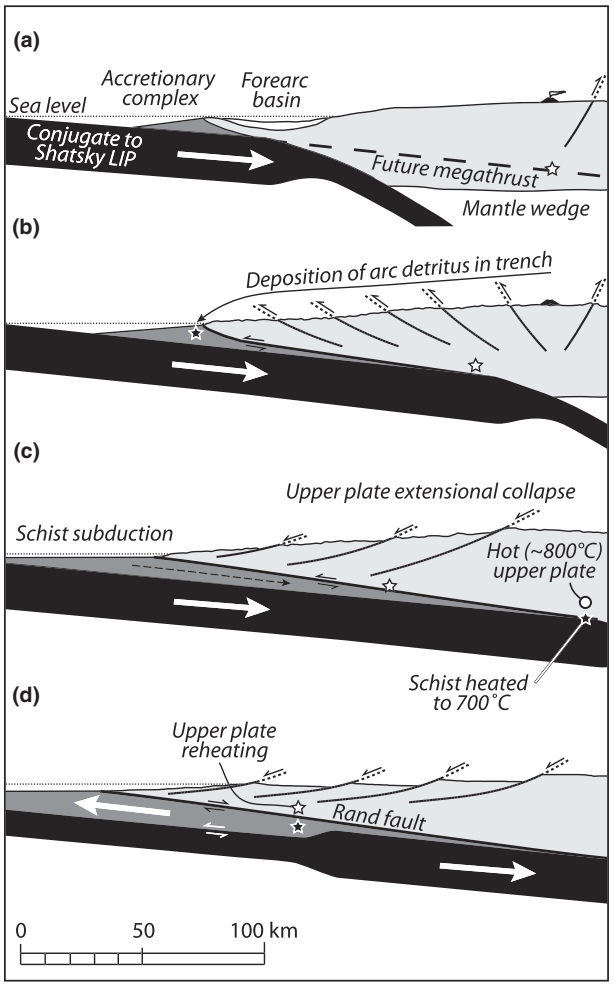

Fig. 16. Generalized cross-section model for the southern SNB. Black and white stars show depositional site of the San Emigdio Schist and native site of the TSE complex, respectively. No vertical exaggeration. (a) Approximately 100 Ma onset of shallow subduction. (b) Approximately 95 Ma upward migration of slab interface to within batholithic crust (base of crust and mantle lithosphere sheared off) and shutoff of arc magmatism. Uplift, contractile deformation, and erosional denudation of the upper plate is followed by deposition and subduction of San Emigdio Schist protolith. (c) Approximately 90 Ma schist underplated beneath recently active arc rocks (~800 °C). Upper plate rocks exposed in San Emigdio and Tehachapi Mountains decompressed from 9 kbar (panel a) to 4 kbar conditions. (d) Approximately 85 Ma. Gravitational collapse of the upper plate drives trench-directed channelized extrusion of the schist (Chapman *et al.*, 2010). Schist flow is dominated by simple shear near the boundaries of the channel and by pure shear at the centre of the wedge. Hot schist juxtaposed with TSE complex, reheating upper plate rocks.

palaeoseismic events (Trepmann & Stöckhert, 2002). Microstructural characteristics of broken garnet (outlined above) and the highly strained texture of host metasandstones are most consistent with deformation-induced garnet fracture, and cannot be explained by alternative mechanisms (e.g. Prior, 1993; Whitney, 1996; Ji *et al*., 1997). High-stress cataclastic deformation of garnet is in conflict with earlier arguments that the schist is not capable of supporting shear stresses in excess of 90 MPa. While the mechanics of brittle failure of rigid inclusions in a ductile matrix are poorly understood, with explanations favouring sequential fracture by high shear stresses at the garnet–matrix interface, the 'modified shear-lag theory' of Ji *et al*. (1997), the phenomenon has long been recognized (e.g. Ramberg, 1955; Boullier, 1980; Mandal *et al*., 2001; Trepmann & Stöckhert, 2002). We suggest a similar mechanism of stress transfer from the weak quartzofeldspathic matrix to the stiff garnet inclusions of the schist.

Fracturing of and deformation twinning in clinopyroxene along the Salinas shear zone are cited as evidence for large (140–1000 MPa), quasi-instantaneous, localized stresses accompanying seismic events (Ducea *et al*., 2007). Deformation twinning in clinopyroxene proceeded in concert with the prograde metamorphic replacement of amphibole by clinopyroxene (Kidder & Ducea, 2006), indicating that seismic events occurred during burial of the schist of Sierra de Salinas to ~10 kbar. Moreover, in the San Emigdio Schist, broken garnet overgrowths are compositionally identical to unbroken garnet rims (cf. Figs 5 & 7), which must have grown during the waning stages of prograde metamorphism at 10 kbar. Therefore, in both Sierra de Salinas and San Emigdio Schist localities, there exists microstructural evidence for large palaeoseismic events, possibly along the subduction megathrust, at ~30 km depth.

If large palaeoseismic events are responsible for cataclastic deformation of San Emigdio Schist garnet, these events must have occurred near peak conditions, i.e. during the reversal from subduction to eduction (Chapman *et al*., 2010). We speculate that stress buildups associated with the reversal in transport polarity resulted in large palaeoseismic events. Numerical simulations indicate that the closure of subduction channels at depth may be characterized by large gradients in stress state (Gerya *et al*., 2002).

Modelling of diffusive relaxation of juxtaposed garnet compositions suggests that garnet from the schist cooled from peak conditions at several 100s °C Myr^{-1}. These cooling rates are consistent with geochronological and thermochronometric studies of the schist (Grove *et al*., 2003, 2008; Saleeby *et al*., 2007; Jacobson *et al*., 2011). In the San Emigdio Schist, the time interval between the youngest detrital zircon U–Pb ages (i.e. the maximum possible depositional age) and muscovite $^{40}Ar/^{39}Ar$ cooling ages is < 3 Myr (Grove *et al*., 2003). Therefore, the schist was subducted to a depth of ~30 km at 700 °C and cooled through the 400 °C closure isotherm for $^{40}Ar/^{39}Ar$ muscovite (McDougall & Harrison, 1999) in < 3 Myr, corresponding to cooling rates of > 100 °C Myr^{-1}. Similar cooling rates (100s °C Myr^{-1}) are fit through high-temperature range garnet and medial range hornblende thermochronometric data from upper plate rocks in the Tehachapi Mountains (Saleeby *et al*., 2007) and are linked to gravitational collapse of the upper plate above the underplated schist (Chapman *et al*., 2010).

Evolution of the thermal structure of a newly initiated flat subduction zone

Field relationships, mineral assemblages, thermobarometry and thermodynamic modelling suggest partial melting of metasandstone San Emigdio Schist under water-saturated conditions. Quartzofeldspathic leucosomes and veins developed during ductile deformation associated with the D1 episode, and are locally overprinted by the D2 fabric. These features indicate that anatexis coincided with ductile deformation near peak conditions, implying that partial melting of metasandstone occurred as the schist reached a maximum depth of subduction (30 km) ~150 km inboard of the trench. We provide here a comparison with subduction complexes in adjacent areas that exhibit evidence for partial melting: the schist of Sierra de Salinas and the Catalina Schist of the California borderland.

Although partial melting probably did not occur in lower-grade Pelona, Orocopia and/or Rand schists, thermobarometric determinations (~700 °C, 10 kbar) and quartzofeldspathic veins and dykes from the schist of Sierra de Salinas suggest that anatexis proceeded under similar pressure, temperature and fluid activity conditions as in the San Emigdio Schist (Kidder & Ducea, 2006; Ducea *et al*., 2009). The timing of schist deposition and metamorphism decreases systematically from north-western (San Emigdio Schist, schists of Sierra de Salinas and Portal Ridge, and Rand Schist) to central and south-eastern exposures (Pelona and Orocopia schists) (Fig. 17) (Grove *et al*., 2003; Jacobson *et al*., 2011). Another distinctive trend not yet recognized is that high reported peak temperatures (590–714 °C) and partial melting are restricted to exposures of the schist with maximum depositional ages between 90 and 80 Ma (Sharry, 1981; Pickett & Saleeby, 1993; Kidder & Ducea, 2006; this study), whereas moderate temperatures (480–575 °C) typify 80–55 Ma schists (Fig. 17) (Graham & England, 1976; Graham & Powell, 1984; Jacobson, 1995, 1997; Jacobson *et al*., 2007). Tectonic underplating and progressive cooling beneath an initially hot upper plate following the onset of shallow subduction may explain this trend. This model also explains partial melting and/or high temperatures in San Emigdio, Tehachapi and Sierra de Salinas schists, lower temperatures in Pelona, Orocopia and Rand schists, inverted metamorphism in the schist as a whole, and the

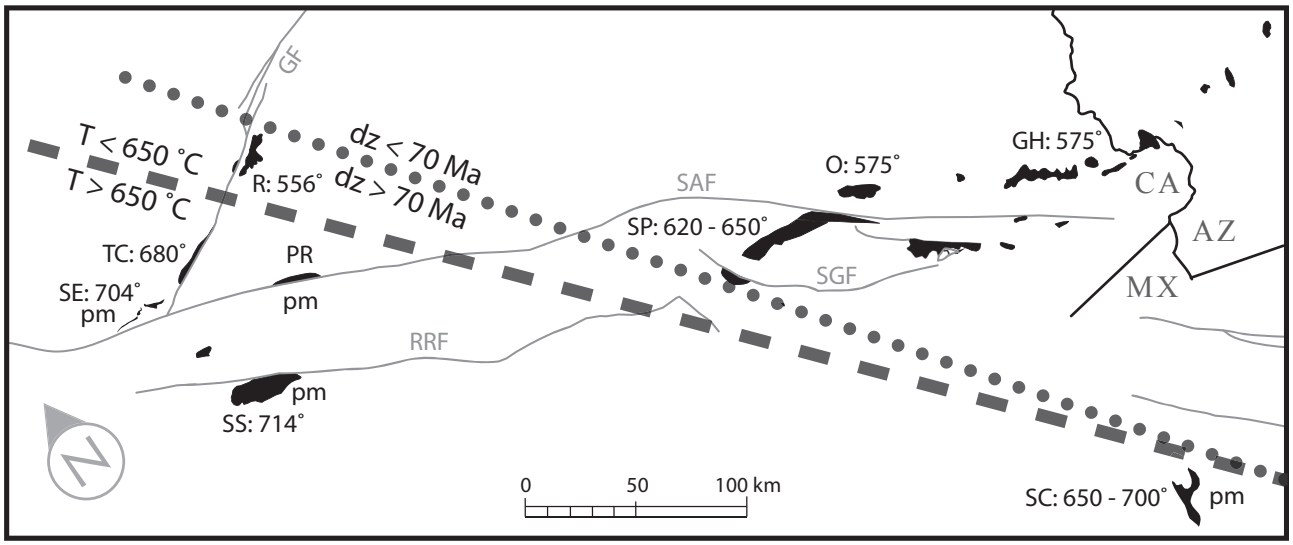

Fig. 17. Palinspastic map showing pre-Neogene positions of San Emigdio and related schist after Grove *et al.* (2003) with 50 km of sinistral slip along the Garlock fault restored (Ross, 1989). Detrital zircon (dz) ages after Grove *et al.* (2003, 2008). Temperatures shown are the highest reported values from individual schist exposures. Temperatures from Sharry (1981) and Pickett & Saleeby (1993) (Tehachapi Mountains); Kidder & Ducea (2006) (Sierra de Salinas); Grove *et al.* (2008) (Santa Catalina Island); Graham & Powell (1984) (Rand Mountains and Sierra Pelona); Oyarzabal (1996) and Jacobson *et al.* (2007) (Orocopia and Gavilan Hills); and this study (San Emigdio Mountains). pm, partial melting; SGF, San Gabriel fault. Other abbreviations as in Fig. 1.

observed *P–T* paths calculated from the San Emigdio body. It could be argued that 80 to 55 Ma schists sit beneath the arc in an inboard position where the upper plate contains younger plutonic rocks than does the upper plate of 90 to 80 Ma schists, and was therefore hotter later. However, Cretaceous to Tertiary plutons are volumetrically minor compared to pre-Cretaceous bodies in the upper plate of 80 to 55 Ma schists (e.g. Jacobson, 1997; Haxel *et al.*, 2002; Jacobson *et al.*, 2007) and we posit that the arc geotherm in the southern Sierra Nevada was higher than that of the Mojave region.

Based on overlapping age and provenance between the San Emigdio Schist and the youngest (*c.* 97–95 Ma), structurally deepest and lowest grade (blueschist and lower-grade facies) portions of the Catalina Schist, a tentative correlation has been assigned (Grove *et al.*, 2008; Jacobson *et al.*, 2011). No correlation is drawn, however, between the San Emigdio Schist and older (*c.* 120–115 Ma), structurally shallow and high-grade (upper amphibolite facies) levels of the Catalina Schist (Grove *et al.*, 2008 and references therein; Jacobson *et al.*, 2011). The top of this inverted metamorphic sequence is characterized by variably migmatized and metasomatized mafic blocks set in a matrix of ultramafic material (Sorensen, 1988). Partial melting in the Catalina Schist is explained by underthrusting of a portion of the Cretaceous forearc beneath the northwestern Peninsular Ranges batholith (Grove *et al.*, 2008). Thrusting within the forearc region proceeded as blueschist and lower-grade varieties were accreted along a comparably long-lived, outboard subduction megathrust. Therefore, similar to the San Emigdio Schist, the Catalina Schist preserves a record of juxtaposing of hot upper plate with relatively cold material and continued underplating of lower-grade units, although accretion of the Catalina Schist occurred over a longer time interval and conceivably along paired subduction megathrusts.

The Catalina Schist, Sierra de Salinas and San Emigdio schists, and subduction-related migmatitic complexes in other areas (e.g. Swakane Gneiss, Matzel *et al.*, 2004; Sierra del Convento mélange, Garcia-Casco *et al.*, 2008) preserve high-pressure/temperature metamorphic parageneses that are inconsistent with those predicted from the thermal structure of steady state subduction (e.g. Peacock, 1987, 2003). These aberrantly high temperatures may be achieved during subduction by some combination of: (i) shear heating (Graham & England, 1976; England & Molnar, 1993); (ii) subduction of hot oceanic lithosphere; (iii) subduction of a spreading centre (e.g. DeLong *et al.*, 1979); (iv) initiation of a new subduction zone (e.g. Platt, 1975; Cloos, 1985; Grove & Bebout, 1995); (v) subduction erosion (e.g. Grove *et al.*, 2008); and (vi) upward migration of the subduction interface (i.e. slab shallowing; Kidder & Ducea, 2006; Ducea *et al.*, 2009). While mechanisms 1, 2 and 3 were probably not significant in the aforementioned terranes (e.g. Kidder & Ducea, 2006), 4, 5 and 6 are favoured for the cases of the Sierra del Convento mélange (Garcia-Casco *et al.*, 2008), Catalina Schist (Grove *et al.*, 2008) and Swakane Gneiss (Matzel *et al.*, 2004), and Sierra de Salinas (Kidder & Ducea, 2006) and San Emigdio schists (Saleeby *et al.*, 2007; Chapman *et al.*, 2010; this study), respectively. A common thread shared by sce-

narios 4–6 is that each places a hot upper plate above a relatively cold lower plate, temporarily raising the geothermal gradient along the interface before steady-state subduction is achieved.

SUMMARY AND CONCLUSIONS

1. Field and petrological relationships for the San Emigdio Schist reveal two episodes of fabric development corresponding to peak (D1) and post-peak (D2) conditions. D1 mineral assemblages and degree of partial melting vary with proximity to the Rand fault, indicating the presence of an inverted metamorphic field gradient. Localized cataclastic deformation of schist garnet and subsequent formation of natural garnet diffusion couples occurred during the D1 episode.
2. Thermobarometric work corroborates petrological evidence for inverted metamorphism in the schist, with peak temperatures increasing from 590 to 700 °C from low to high structural levels, corresponding to thermal gradients of 50–240 °C km^{-1}. Peak pressures range from 8.5 to 11.1 kbar and do not vary with structural depth. Temperatures calculated from the San Emigdio gneiss (675–710 °C) are identical within error to those from the uppermost levels of the schist, whereas calculated pressures are ~1 kbar lower (7.1–8.4 kbar).
3. Thermodynamic modelling constrains the *P–T* history of the schist, which probably involved retrogression along a similar trajectory as the prograde path, resulting in a 'Franciscan-type' *P–T* path.
4. Diffusion modelling of natural garnet couples indicates rapid (825–380 °C Myr^{-1}) cooling from peak conditions to ~500 °C.

These data constrain the *P–T* history and the tectonics of underplating and exhumation of the San Emigdio Schist. This involved: (i) subduction and progressive underplating of the primarily turbiditic and basaltic schist protolith and the development of an inverted metamorphic gradient; (ii) low volume partial melting in the schist at peak conditions; (iii) localized fracture of garnet at high stresses and strain rates immediately prior to peak conditions, possibly related to large subduction zone seismic events; and (iv) reheating of upper plate batholithic assemblages during rapid structural ascent of the schist. While these results are consistent with an inferred tectonic evolution from shallow subduction beneath the recently active Late Cretaceous arc to exhumation by rapid trench-directed channelized extrusion in the subducted schist (Chapman *et al.*, 2010), we cannot preclude alternative models solely based on this study.

We document the physical conditions fossilized in a deeply exhumed subduction channel in an ancient flat slab system. This research should facilitate future recognition of analogous ancient systems in other orogenic belts. Continued understanding of the dynamics of flat subduction requires a highly interactive approach between observational geophysics, dynamic modelling and geological observation of both active and ancient systems.

ACKNOWLEDGEMENTS

This research was supported by National Science Foundation grant EAR-0739071 and by the Gordon and Betty Moore Foundation. This is Caltech Tectonics Observatory Contribution 146. The manuscript benefitted from discussions with N. Borneman, E. Dachs, J. Eiler, Y. Guan, C. Jacobson, S. Kidder and D. Vielzeuf. A.Barth, J. Platt and D. Whitney are thanked for thoughtful reviews of the manuscript.

REFERENCES

Barth, A.P., Wooden, J.L., Grove, M., Jacobson, C.E. & Pedrick, J.N., 2003. U-Pb zircon geochronology of rocks in the Salinas Valley region of California; a reevaluation of the crustal structure and origin of the Salinian Block. *Geology*, **31,** 517–520.

Boullier, A.M., 1980. A preliminary study on the behaviour of brittle minerals in a ductile matrix: example of zircons and feldspars. *Journal of Structural Geology*, **2,** 211–217.

Chakraborty, S. & Ganguly, J., 1991. Compositional zoning and cation diffusion in garnets. *Advances in Physical Geochemistry*, **8,** 120–175.

Chakraborty, S. & Ganguly, J., 1992. Cation diffusion in aluminosilicate garnets; experimental determination in spessartine-almandine diffusion couples, evaluation of effective binary, diffusion coefficients, and applications. *Contributions to Mineralogy and Petrology*, **111,** 74–86.

Chapman, A.D., Luffi, P. & Saleeby, J.B., 2006. The origin of high-Ca annuli in garnets from the Rand Schist of the San Emigdio Mountains, Southern California. *Eos, Transactions, American Geophysical Union*, **87,** Fall Meeting Supplement, Abstract V31B-0588.

Chapman, A.D., Kidder, S., Saleeby, J. & Ducea, M., 2010. Role of extrusion of the Rand and Sierra de Salinas schists in Late Cretaceous extension and rotation of the southern Sierra Nevada and vicinity. *Tectonics*, **29,** TC5006, doi:10.1029/2009TC002597.

Chernoff, C.B. & Carlson, W.D., 1999. Trace element zoning as a record of chemical disequilibrium during garnet growth. *Geology*, **27,** 555–558.

Cloos, M., 1982. Flow melanges; numerical modeling and geologic constraints on their origin in the Franciscan subduction complex, California. *Geological Society of America Bulletin*, **93,** 330–344.

Cloos, M., 1985. Thermal evolution of convergent plate margins; thermal modeling and reevaluation of isotopic Ar-ages for blueschists in the Franciscan Complex of California. *Tectonics*, **4,** 421–433.

Crowell, J.C., 1952. Geology of the Lebec Quadrangle, California. *Special Report – California Division of Mines and Geology*, **24,** 1–24.

Dachs, E. & Proyer, A., 2002. Constraints on the duration of high-pressure metamorphism in the Tauern Window from diffusion modelling of discontinuous growth zones in eclogite garnet. *Journal of Metamorphic Geology*, **20,** 769–780.

DeLong, S.E., Schwarz, W.M. & Anderson, R.N., 1979. Thermal effects of ridge subduction. *Earth and Planetary Science Letters*, **44,** 239–246.

Dibblee, T.W., 1973. Geologic maps of the Santiago Creek, Eagle Rest Peak, Pleito Hills, Grapevine, and Pastoria Creek quadrangles, Kern County, California. *U.S. Geological Survey Open File Report 73-57*.

Dibblee, T.W., 1986. Geology of the San Emigdio Mountains, California. *Field Trip Guidebook – Pacific Section, Society of Economic Paleontologists and Mineralogists*, **48,** 1–10.

Ducea, M.N., Kidder, S. & Chesley, J.T., 2007. A geologic window into a subduction megathrust. *Eos, Transactions, American Geophysical Union*, **88,** 277 pp.

Ducea, M.N., Kidder, S., Chesley, J.T. & Saleeby, J.B., 2009. Tectonic underplating of trench sediments beneath magmatic arcs; the Central California example. *International Geology Review*, **51,** 1–26.

Ehlig, P.L., 1981. Origin and tectonic history of the basement terrane of the San Gabriel Mountains, central Transverse Ranges. In: *The Geotectonic Development of California, Rubey Volume I* (ed. Ernst, W.G.), pp. 253–283. Prentice-Hall, Englewood Cliffs, NJ.

England, P. & Molnar, P., 1993. The interpretation of inverted metamorphic isograds using simple physical calculations. *Tectonics*, **12,** 145–158.

English, J.M., Johnston, S.T. & Wang, K., 2003. Thermal modelling of the Laramide Orogeny; testing the flat-slab subduction hypothesis. *Earth and Planetary Science Letters*, **214,** 619–632.

Ernst, W.G., 1988. Tectonic history of subduction zones inferred from retrograde blueschist *P-T* paths. *Geology*, **16,** 1081–1084.

Escuder Viruete, J., Indares, A. & Arenas, R., 2000. *P-T* paths derived from garnet growth zoning in an extensional setting; an example from the Tormes gneiss dome (Iberian Massif, Spain). *Journal of Petrology*, **41,** 78 pp.

Ganguly, J., 2002. Diffusion kinetics in minerals: Principles and applications to tectono-metamorphic processes. *European Mineralogical Union, Notes in Mineralogy*, **4,** 271–309.

Ganguly, J., Bhattacharya, R.N. & Chakraborty, S., 1988. Convolution effect in the determination of composition profiles and diffusion coefficients by microprobe step scans. *American Mineralogist*, **73,** 901–909.

Ganguly, J., Cheng, W. & Tirone, M., 1996. Thermodynamics of aluminosilicate garnet solid solution; new experimental data, an optimized model, and thermometry applications. *Contributions to Mineralogy and Petrology*, **126,** 137–151.

Garcia-Casco, A., Lazaro, C., Rojas-Agramonte, Y. *et al*., 2008. Partial melting and counterclockwise *P-T* path of subducted oceanic crust (Sierra del Convento Melange, Cuba). *Journal of Petrology*, **49,** 129–161.

Gerya, T.V., Stöckhert, B. & Perchuk, A.L., 2002. Exhumation of high-pressure metamorphic rocks in a subduction channel; a numerical simulation. *Tectonics*, **21,** 19 pp.

Glicksman, M.E., 2000. *Diffusion in Solids: Field Theory, Solid-State Principles, and Applications*. Wiley, New York.

Graham, C.M. & England, P.C., 1976. Thermal regimes and regional metamorphism in the vicinity of overthrust faults; an example of shear heating and inverted metamorphic zonation from southern California. *Earth and Planetary Science Letters*, **31,** 142–152.

Graham, C.M. & Powell, R., 1984. A garnet-hornblende geothermometer; calibration, testing, and application to the Pelona Schist, Southern California. *Journal of Metamorphic Geology*, **2,** 13–31.

Grove, M. & Bebout, G.E., 1995. Cretaceous tectonic evolution of coastal Southern California; insights from the Catalina Schist. *Tectonics*, **14,** 1290–1308.

Grove, M., Jacobson, C.E., Barth, A.P. & Vucic, A., 2003. Temporal and spatial trends of Late Cretaceous-early Tertiary underplating Pelona and related schist beneath Southern California and southwestern Arizona. *Geological Society of America Special Paper*, **374,** 381–406.

Grove, M., Bebout, G.E., Jacobson, C.E. *et al*., 2008. The Catalina Schist; evidence for Middle Cretaceous subduction erosion of southwestern North America. *Geological Society of America Special Paper*, **436,** 335–361.

Guiraud, M., Powell, R. & Rebay, G., 2001. H_2O in metamorphism and unexpected behaviour in the preservation of metamorphic mineral assemblages. *Journal of Metamorphic Geology*, **19,** 445–454.

Gutscher, M.-A., Spakman, W., Bijwaard, H. & Engdahl, E.R., 2000. Geodynamics of flat subduction; seismicity and tomographic constraints from the Andean margin. *Tectonics*, **19,** 814–833, doi:10.1029/1999TC001152.

Haxel, G.B. & Dillon, J.T., 1978. The Pelona-Orocopia Schist and Vincent–Chocolate Mountain thrust system, southern California. In: *Mesozoic paleogeography of the western United States: Los Angeles, Society of Economic Paleontologists and Mineralogists Pacific Section Pacific Coast Paleogeography Symposium 2* (eds Howell, D.G. & McDougall, K.A.), pp. 453–469.

Haxel, G.B., Jacobson, C.E., Richard, S.M., Tosdal, R.M. & Grubensky, M.J., 2002. The Orocopia Schist in southwest Arizona: Early Tertiary oceanic rocks trapped or transported far inland. In: *Contributions to Crustal Evolution of the Southwestern United States* (ed. Barth, A.). *Geological Society of America Special Paper*, **365,** 99–128.

Holland, T.J.B. & Powell, R., 1998. An internally consistent thermodynamic data set for phases of petrological interest. *Journal of Metamorphic Geology*, **16,** 309–343.

Jacobson, C.E., 1983. Structural geology of the Pelona Schist and Vincent Thrust, San Gabriel Mountains, California. *Geological Society of America Bulletin*, **94,** 753–767.

Jacobson, C.E., 1995. Qualitative thermobarometry of inverted metamorphism in the Pelona and Rand schists, Southern California, using calciferous amphibole in mafic schist. *Journal of Metamorphic Geology*, **13,** 79–92.

Jacobson, C.E., 1997. Metamorphic convergence of the upper and lower plates of the Vincent Thrust, San Gabriel Mountains, Southern California, USA. *Journal of Metamorphic Geology*, **15,** 155–165.

Jacobson, C.E., Dawson, M.R. & Postlethwaite, C.E., 1988. Structure, metamorphism, and tectonic significance of the Pelona, Orocopia, and Rand schists, Southern California. In: *Metamorphism and Crustal Evolution of the Western United States, Rubey Volume* (ed. Ernst, W.G.), pp. 976–997. Prentice-Hall, Englewood Cliffs, NJ.

Jacobson, C.E., Oyarzabal, F.R. & Haxel, G.B., 1996. Subduction and exhumation of the Pelona-Orocopia-Rand schists, Southern California. *Geology*, **24,** 547–550.

Jacobson, C.E., Grove, M., Stamp, M.M. *et al*., 2002. Exhumation history of the Orocopia Schist and related rocks in the Gavilan Hills area of southeasternmost California. *Geological Society of America Special Paper*, **365,** 129–154.

Jacobson, C.E., Grove, M., Vucic, A., Pedrick, J.N. & Ebert, K.A., 2007. Exhumation of the Orocopia Schist and associated rocks of southeastern California; relative roles of erosion, synsubduction tectonic denudation, and middle Cenozoic extension. *Geological Society of America Special Paper*, **419,** 1–37.

Jacobson, C.E., Grove, M., Pedrick, J.N. *et al*., 2011. Late Cretaceous–early Cenozoic tectonic evolution of the southern California margin inferred from provenance of trench and forearc sediments. *Geological Society of America Bulletin*, **123,** 485–506, doi: 10.1130/B30238.1.

James, E.W., 1986. *Geochronology, Isotopic Characteristics, and Paleogeography of Parts of the Salinian Block of California*. PhD thesis, University of California, Santa Barbara.

Jamieson, R.A., Beaumont, C., Hamilton, J. & Fullsack, P., 1996. Tectonic assembly of inverted metamorphic sequences. *Geology*, **24,** 839–842.

Ji, S., Zhao, P. & Saruwatari, K., 1997. Fracturing of garnet crystals in anisotropic metamorphic rocks during uplift. *Journal of Structural Geology*, **19,** 603–620.

Karato, S., Wang, Z., Liu, B. & Fujino, K., 1995. Plastic deformation of garnets: systematics and implications for the rheology of the mantle transition zone. *Earth and Planetary Science Letters*, **130,** 13–30.

Kidder, S. & Ducea, M.N., 2006. High temperatures and inverted metamorphism in the schist of Sierra de Salinas,

California. *Earth and Planetary Science Letters*, **241,** 422–437.
Kidder, S., Ducea, M., Gehrels, G., Patchett, P.J. & Vervoort, J., 2003. Tectonic and magmatic development of the Salinian Coast Ridge Belt, California. *Tectonics*, **22,** 1058, doi:10.1029/2002TC001409.
Kincaid, C. & Sacks, I.S., 1997. Thermal and dynamical evolution of the upper mantle in subduction zones. *Journal of Geophysical Research*, **102,** 12,295–12,315.
Kistler, R.W. & Champion, D.E., 2001. Rb-Sr whole-rock and mineral ages, K-Ar, $^{40}Ar/^{39}Ar$, and U-Pb mineral ages, and strontium, lead, neodymium, and oxygen isotopic compositions for granitic rocks from the Salinian Composite Terrane, California. *U.S. Geological Survey Open File Report 01-453*, 84 pp.
Kohn, M.J. & Spear, F., 2000. Retrograde net transfer reaction insurance for pressure-temperature estimates. *Geology*, **28,** 1127–1130.
Konrad-Schmolke, M., Handy, M.R., Babist, J. & O'Brien, P.J., 2005. Thermodynamic modeling of diffusion-controlled garnet growth. *Contributions to Mineralogy and Petrology*, **149,** 181–195.
Krogh, E.J., Oh, C.W. & Liou, J.G., 1994. Polyphase and anticlockwise *P-T* evolution for Franciscan eclogites and blueschists from Jenner, California, USA. *Journal of Metamorphic Geology*, **12,** 121–134.
Liu, L., Spasojevic, S. & Gurnis, M., 2008. Reconstructing Farallon Plate subduction beneath North America back to the Late Cretaceous. *Science*, **322,** 934–938, doi:10.1126/science.1162921.
Liu, L., Gurnis, M., Seton, M., Saleeby, J., Müller, R.D. & Jackson, J.M., 2010. The role of oceanic plateau subduction in the Laramide orogeny. *Nature Geoscience*, **3,** 353–357, doi:10.1038/NGEO829.
Ludington, S., Moring, B., Miller, R.J. *et al*., 2007. Preliminary integrated geologic map databases for the United States. *U.S. Geological Survey Open File Report 2005-1305*. Version 1.3, original file updated in December 2007. Available at: http://pubs.usgs.gov/of/2005/1305/index.htm.
Mandal, N., Chakraborty, C. & Samanta, S.K., 2001. Controls on the failure mode of brittle inclusions hosted in a ductile matrix. *Journal of Structural Geology*, **23,** 51–66, doi:10.1016/S0191-8141(00)00127-9.
Matzel, J.E.P., Bowring, S.A. & Miller, R.B., 2004. Protolith age of the Swakane Gneiss, north Cascades, Washington; evidence of rapid underthrusting of sediments beneath an arc. *Tectonics*, **23,** 18 pp.
McDougall, I. & Harrison, T.M., 1999. *Geochronology and Thermochronology by the 40Ar/*39Ar Method. Oxford University Press, New York, 269 pp.
McNulty, B. & Farber, D., 2002. Active detachment faulting above the Peruvian flat slab. *Geology*, **30,** 567–570.
Oyarzabal, F.R., 1996. *Metamorphic History and Structural Evolution of the Orocopia Schist in the Gavilan Hills, S.E.* PhD thesis, Iowa State University, Ames.
Oyarzabal, F.R., Jacobson, C.E. & Haxel, G.B., 1997. Extensional reactivation of the Chocolate Mountains subduction thrust in the Gavilan Hills of southeastern California. *Tectonics*, **16,** 650–661.
Pardavi-Horváth, M., 1984. Microhardness and brittle fracture of garnet single crystals. *Journal of Materials Science*, **19,** 1159–1170.
Peacock, S.M., 1987. Thermal effects of metamorphic fluids in subduction zones. *Geology*, **15,** 1057–1060.
Peacock, S.M., 1992. Blueschist-facies metamorphism, shear heating, and *P-T-t* paths in subduction shear zones. *Journal of Geophysical Research*, **97,** 17,693–17,707.
Peacock, S.M., 2003. Thermal structure and metamorphic evolution of subducting slabs. In: *Geophysical Monograph* (ed. Eiler, J.M.), vol. 138, pp. 7–22. AGU, Washington, D.C.
Perchuk, A., Philippot, P., Erdmer, P. & Fialin, M., 1999. Rates of thermal equilibration at the onset of subduction deduced from diffusion modeling of eclogitic garnets, Yukon-Tanana Terrane, Canada. *Geology*, **27,** 531–534.
Pickett, D.A. & Saleeby, J.B., 1993. Thermobarometric constraints on the depth of exposure and conditions of plutonism and metamorphism at deep levels of the Sierra Nevada Batholith, Tehachapi Mountains, California. *Journal of Geophysical Research*, **98,** 609–629.
Pickett, D.A. & Saleeby, J.B., 1994. Nd, Sr, and Pb isotopic characteristics of Cretaceous intrusive rocks from deep levels of the Sierra Nevada Batholith, Tehachapi Mountains, California. *Contributions to Mineralogy and Petrology*, **118,** 198–215, doi:10.1007/BF01052869.
Platt, J.P., 1975. Metamorphic and deformational processes in the Franciscan Complex, California; some insights from the Catalina Schist terrane. *Geological Society of America Bulletin*, **86,** 1337–1347.
Postlethwaite, C.E. & Jacobson, C.E., 1987. Early history and reactivation of the Rand Thrust, Southern California. *Journal of Structural Geology*, **9,** 195–205, doi:10.1016/0191-8141(87)90025-3.
Powell, R. & Holland, T., 1994. Optimal geothermometry and geobarometry. *American Mineralogist*, **79,** 120–133.
Prior, D.J., 1993. Sub-critical fracture and associated retrogression of garnet during mylonitic deformation. *Contributions to Mineralogy and Petrology*, **113,** 545–556.
Ramberg, H., 1955. Natural and experimental boudinage and pinch-and-swell structures. *Journal of Geology*, **63,** 512–526.
Ross, D.C., 1989. The metamorphic and plutonic rocks of the southernmost Sierra Nevada, California, and their tectonic framework. *U.S. Geological Survey Professional Paper 1381*, 159 pp.
Saleeby, J., 2003. Segmentation of the Laramide slab; evidence from the southern Sierra Nevada region. *Geological Society of America Bulletin*, **115,** 655–668.
Saleeby, J.B., Sams, D.B. & Kistler, R.W., 1987. U/Pb zircon, strontium, and oxygen isotopic and geochronological study of the southernmost Sierra Nevada Batholith, California. *Journal of Geophysical Research*, **92,** 10,443–10,466.
Saleeby, J., Farley, K.A., Kistler, R.W. & Fleck, R.J., 2007. Thermal evolution and exhumation of deep-level batholithic exposures, southernmost Sierra Nevada, California. *Geological Society of America Special Paper*, **419,** 39–66.
Sharry, J., 1981. *The Geology of the Western Tehachapi Mountains, California*. PhD thesis, Massachusetts Institute of Technology, Cambridge.
Sorensen, S.S., 1988. Petrology of amphibolite-facies mafic and ultramafic rocks from the Catalina Schist, Southern California; metasomatism and migmatization in a subduction zone metamorphic setting. *Journal of Metamorphic Geology*, **6,** 405–435.
Spear, F.S., 1993. *Metamorphic Phase Equilibria and Pressure-Temperature-Time Paths*. Mineralogical Society of America, Washington, DC, 799 pp.
Spear, F.S. & Selverstone, J., 1983. Quantitative *P-T* path from zoned minerals; theory and tectonic applications. *Contributions to Mineralogy and Petrology*, **83,** 348–357.
Trepmann, C.A. & Stöckhert, B., 2002. Cataclastic deformation of garnet; a record of synseismic loading and postseismic creep. *Journal of Structural Geology*, **24,** 1845–1856.
Vance, D. & Mahar, E., 1998. Pressure-temperature paths from *P-T* pseudosections and zoned garnets; potential, limitations and examples from the Zanskar Himalaya, NW India. *Contributions to Mineralogy and Petrology*, **132,** 225–245.
Vielzeuf, D., Baronnet, A., Perchuk, A.L., Laporte, D. & Baker, M.B., 2007. Calcium diffusivity in alumino-silicate garnets; an experimental and ATEM study. *Contributions to Mineralogy and Petrology*, **154,** 153–170.
Wakabayashi, J., 1990. Counterclockwise *P-T-t* paths from amphibolites, Franciscan Complex, California; relics from the early stages of subduction zone metamorphism. *Journal of Geology*, **98,** 657–680.

Wakabayashi, J. & Dumitru, T.A., 2007. $^{40}Ar/^{39}Ar$ Ages from coherent, high-pressure metamorphic rocks of the Franciscan Complex, California: revisiting the timing of metamorphism of the world's type subduction complex. *International Geology Review*, **49,** 873–906.

Whitney, D.L., 1996. Garnets as open systems during regional metamorphism. *Geology*, **24,** 147–150.

Whitney, D.L., Broz, M. & Cook, R.F., 2007. Hardness, toughness, and modulus of some common metamorphic minerals. *American Mineralogist*, **92,** 281–288, doi:10.2138/am.2007.2212.

Wood, D.J. & Saleeby, J.B., 1997. Late Cretaceous–Paleocene extensional collapse and disaggregation of the southernmost Sierra Nevada Batholith. *International Geology Review*, **39,** 973–1009, doi:10.1080/00206819709465314.

Yin, A., 2002. Passive-roof thrust model for the emplacement of the Pelona-Orocopia Schist in Southern California, United States. *Geology*, **30,** 183–186.

SUPPORTING INFORMATION

Additional Supporting Information may be found in the online version of this article:

Appendix S1. Descriptions of modelling techniques.

Appendix S2. Listing of numbered fields in Figs 10 and 14.

Table S1. Representative garnet analyses used in thermobarometric calculations (normalized to 12 O). Ferric iron calculated using the program AX (Holland & Powell, 1998). m, mafic schist; s, metasandstone schist; seg, San Emigdio gneiss.

Table S2. Representative biotite analyses used in thermobarometric calculations (normalized to eight cations). Ferric iron calculated using the program AX (Holland & Powell, 1998). Abbreviations as in Table S1.

Table S3. Representative muscovite analyses used in thermobarometric calculations (normalized to seven cations). Ferric iron calculated using the program AX (Holland & Powell, 1998). Abbreviations as in Table S1.

Table S4. Representative plagioclase analyses used in thermobarometric calculations (normalized to 8 O). Ferric iron calculated using the program AX (Holland & Powell, 1998). Abbreviations as in Table S1.

Table S5. Representative amphibole analyses used in thermobarometric calculations (normalized to 23 O). Ferric iron calculated using the program AX (Holland & Powell, 1998). Abbreviations as in Table S1.

Table S6. Bulk compositions of San Emigdio Schist from XRF analyses. 'Prograde' compositions are H_2O-saturated. 'Retrograde' compositions are H_2O-saturated and modified by subtracting garnet from 'prograde' compositions. Abbreviations as in Table S1.

Please note: Wiley–Blackwell are not responsible for the content or functionality of any supporting materials supplied by the authors. Any queries (other than missing material) should be directed to the corresponding author for the article.

Received 9 August 2010; revision accepted 24 January 2011.